

## Research papers

## A directly charged thermal store for compressed air energy storage systems

Bruno Cárdenas<sup>\*</sup>, Seamus Garvey

Department of Mechanical, Materials and Manufacturing Engineering, University of Nottingham, University Park, Nottingham NG7 2RD, United Kingdom



## ARTICLE INFO

## Keywords:

CAES  
High temperature thermal storage  
Directly charged thermal store  
Thermocline  
Packed bed  
Granular media heat storage

## ABSTRACT

This paper discusses the design of a heat storage unit with integrated heat exchangers (TES + HX), which is intended to work in a Compressed Air Energy Storage (CAES) system. The unit can be charged directly by the system's stream of pressurised air, eliminating the need for additional heat exchangers and reducing the number of heat transfer processes. Silica sand is used as the storage medium due to its high heat capacity, non-corrosivity and its ability to accommodate the thermal expansion of steel pipes.

A medium-scale, medium-duration CAES system (250 kW/1MWh) is used as a case study. The heat storage subsystem comprises a packed-bed thermal store, three air-to-air heat exchangers and an ambient pressure air blower. Combined, this subsystem has an approximate cost of £147k and achieves an efficiency of ~89 %, which translates into a levelized cost of ~48.5 £/MWh. An integrated TES + HX unit can achieve a levelized cost of ~35 £/MWh. The unit has an estimated cost of £38.5k and achieves an overall roundtrip exergy efficiency of ~91.8 %. The integrated TES + HX unit not only offers a significant reduction in the capital cost of a CAES system and an efficiency improvement, but it also allows for a simpler overall architecture.

## 1. Introduction

Compressed air energy storage (CAES) systems have been the subject of substantial research in recent years [1–11]. They are considered as one of the main grid-scale energy storage technologies that can be used to provide flexibility in future renewable-dominated electricity networks [12,13].

Renewable generation is not only intermittent, but it is also inflexible. Therefore, the grid loses flexibility as it incorporates more renewables, and the task of balancing generation and demand becomes more challenging [14].

Energy storage provides a solution to this problem by taking 'excess' electricity from the grid and storing it. This electricity is returned to the grid when demand exceeds generation. Energy storage technologies enable integrating a large share of renewables into the grid and are key to achieve a zero-emission electricity system [15].

In this work we consider a high-temperature CAES system. This system stores electricity (exergy) in the form of high-grade heat and pressure. Fig. 1 shows a basic schematic of this type of system.

During a charging cycle a CAES system uses electricity from the grid to compress ambient air up to a high pressure. Typical storage pressures are around 250 bar, which are accomplished through multiple compression stages.

The incoming stream of ambient air is preheated to ~214 °C before entering the compression train. The air emerges at ~550 °C from each stage of compression and is cooled back down to 214 °C in an air-to-air heat exchanger (HX).

After the final stage of compression, the compressed air flows through a recuperator to preheat the incoming ambient air. Finally, the compressed air is stored at ambient temperature in a pressure reservoir.

## Nomenclature

## Acronyms

<i>ID</i>	Pipe internal diameter (m)
<i>CAES</i>	Compressed Air Energy Storage
<i>L</i>	Length of TES + HX unit container and of the pipes in the array (m)
<i>CSP</i>	Concentrated Solar Power
<i>LCoS</i>	Levelised cost of storage (£/MWh)
<i>HTF</i>	Heat Transfer Fluid
<i>m</i>	Total mass flow of air passing through unit, across all pressure levels (kg/s)
<i>HX</i>	Heat Exchanger
<i>m<sub>per pipe</sub></i>	Air mass flow rate per pipe (kg/s)

<sup>\*</sup> Corresponding author.

E-mail address: [bruno.cardenas@nottingham.ac.uk](mailto:bruno.cardenas@nottingham.ac.uk) (B. Cárdenas).

<i>TES</i>	Thermal Energy Store
<i>Mass<sub>Steel</sub></i>	Mass of steel used for the construction of the unit (kg)
<i>TES + HX</i>	Thermal Energy Store with integrated heat exchanger(s)
<i>N</i>	Number of axial elements in FEA model

**Variables**

<i>No<sub>Pipes</sub></i>	Number of pipes in the array
$\alpha$	Cost of the steel used (£/kg)
<i>Nu</i>	Nusselt number
$\beta$	Cost per mm of welding (£/mm)
<i>OD</i>	Outer diameter of pipes (m)
$\gamma$	Cost of x-ray inspection per welded joint (£/joint)
<i>P<sub>in</sub></i>	Pressure of a given stream of compressed air entering the TES + HX unit (Pa)
$\eta$	Roundtrip exergy efficiency
<i>P<sub>out</sub></i>	Outlet pressure of a given stream of compressed air emerging from TES + HX unit (Pa)
$\lambda$	Lifetime of the TES + HX unit (Years)
<i>P<sub>max</sub></i>	Maximum pressure in the system (Pa)
$\mu$	Dynamic viscosity of air (Pa·s)
<i>Pr</i>	Prandtl number
$\rho$	Density air (kg/m <sup>3</sup> )
<i>r</i>	Compression ratio of CAES system (250 <sup>1/3</sup> )
$\varphi$	Used for calculation of friction factor
<i>R<sub>air</sub></i>	Gas constant for air (287.05 J/kg·K)
$\Omega$	Allowable pressure exergy loss as a fraction of pressure exergy input during charge
<i>Re</i>	Reynold's number
<i>A</i>	Heat-exergy content (above 214 °C) of the outlet air during the discharge cycle (kWh)
<i>rough<sub>rel</sub></i>	Relative roughness of pipes
<i>AR</i>	Aspect ratio of the unit (length/height)
<i>S</i>	Allowable stress of steel (MPa)
<i>B</i>	Pressure-exergy available after losses during charge and discharge (kWh)
<i>Spacing</i>	Spacing between heat transfer discs (mm)
<i>Capex</i>	Capital cost of hardware (£)
<i>Stage Pressure</i>	Pressure of air stream (Pa)
<i>Charging Cost</i>	Cost of the exergy put into storage (£)
<i>t</i>	Duration of work cycle in seconds (s)
<i>Cost<sub>Steel</sub></i>	Total cost of the steel used for the construction of the unit (£)
<i>T<sub>0</sub></i>	Ambient temperature (20 °C)
<i>Cost<sub>welding</sub></i>	Total cost of welding pipes to manifolds on both ends of unit (£)
<i>T<sub>in</sub></i>	Inlet temperature for the TES + HX unit (K)
<i>Cost<sub>xray</sub></i>	Total cost for x-ray inspection of welded joints (£)
<i>T<sub>max</sub></i>	Temperature of compressor outlet & max temp. of hot side of TES + HX unit (°C)
<i>Cp</i>	Specific heat capacity (kJ/kg·K)
<i>v</i>	Velocity of air flow (m/s)
<i>d</i>	Heat transfer disc thickness (mm)
<i>Wall<sub>Thick</sub></i>	Thickness of pipe's wall (mm)
$\Delta T$	Temperature difference (K)
<i>W<sub>H</sub></i>	Heat-Exergy put into the thermal store during a charge cycle (kWh)
$\Delta P$	Pressure drop throughout a length of pipe (Pa)
<i>W<sub>P</sub></i>	Total pressure-exergy that passes through the TES + HX unit during a charge cycle (kWh)
<i>f</i>	Friction factor
<i>x</i>	Discount rate (5 %)
<i>flow<sub>area</sub></i>	Cross sectional area of pipe centre (m <sup>2</sup> )
<i>z</i>	Rate of change of heat transfer area provided by discs with respect to spacing

The stream of ambient pressure air flowing through the 3 HXs takes

the heat of compression to a dedicated thermal store (TES). In most CAES, the TES is a non-pressurised packed bed of rocks.

This secondary stream of air enters the TES container through the top where it comes in direct contact with the rocks. The air transfers its heat to the rocks as it flows downwards along the container. Heat is stored in the TES with a thermal gradient, which in this case goes from ~550 °C at the top down to ~214 °C at the bottom.

To discharge the stored exergy, the process is reversed. Compressed air is released from the pressure reservoir and reheated using the heat stored in the TES. The compressed air is expanded in multiple stages, with reheating between each stage. After the final expansion, the air flows through the recuperator where it surrenders the remainder of its heat content before being vented to ambient.

In a high-temperature CAES system with a rated discharge power of 250 kW and 1MWh of storage capacity, the heat exchangers would have an approximate cost of ~£100k (excluding the recuperator) while a packed bed type TES could be fabricated for ~£40k.

**1.1. Objective**

This paper explores the possibility of integrating the thermal store with the heat exchangers of the system into a single unit that performs both functions. An integrated TES + HX can reduce the overall cost of the system and it can also reduce the footprint of the system. In turn this can boost the deployment of CAES systems.

In theory, one possible way to realize this integrated unit is to circulate compressed air directly through the TES container. However, this presents 2 major problems: *i*) the thermal store would need to be a pressure vessel and *ii*) multiple pressure-resistant containers would be

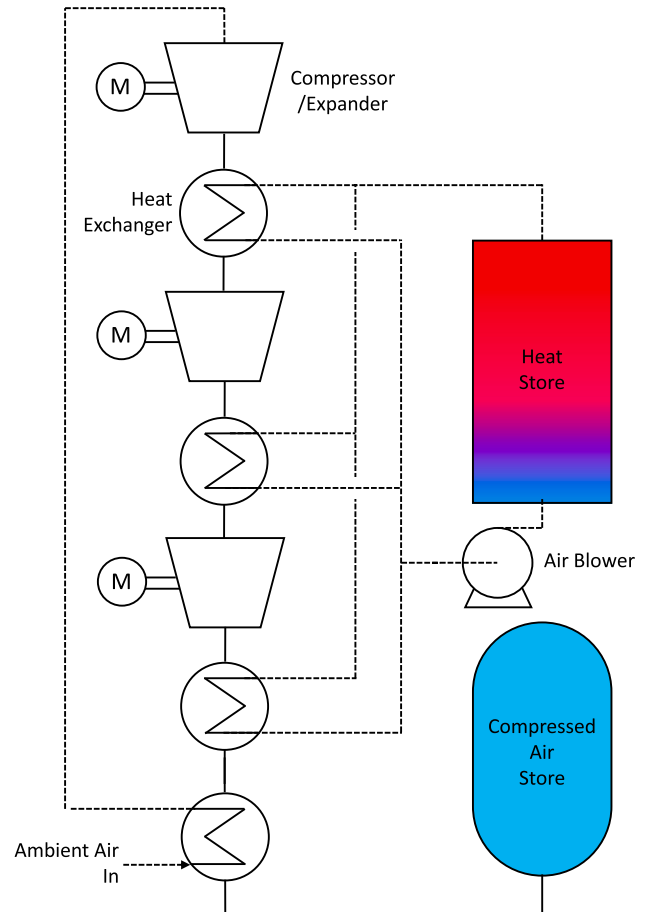


**Fig. 1.** Schematic of a high-temperature adiabatic compressed air energy storage system.

needed due to the different pressure levels in the system.

A vessel of such dimensions and rated to operate at high temperatures and relatively high pressures would be prohibitively expensive. Therefore, removing the HXS from the system in this way is simply not economically viable.

## 2. Background

Considerable work has been carried out in recent years on ambient-pressure, thermal stores (packed beds) which are charged indirectly by a secondary stream of air or another heat transfer fluid. Examples of this stream of work can be found in [16–26]. Very limited work exists on directly charged heat stores. The concepts reviewed here were developed for concentrated solar power (CSP) plants; however, the operating principles and challenges are similar.

The DLR in Germany studied using concrete as a high temperature heat storage material for parabolic trough solar plants [27]. Fig. 2 shows a prototype unit consisting of an array of tubes embedded in a concrete block. The array of tubes consists of 132 tubes with an outer diameter of 18 mm, which were rated for 25 bar and 400 °C. The tubes are connected to a manifold at each end of the unit. Pressurised steam was used as the heat transfer fluid (HTF). The concrete block has a total length of 12.6 m, a width of 1.35 and a height of 1.32 m [28].

The module was tested for >13,000 h and carried out almost 600 thermal cycles. A satisfactory performance was observed during the tests. It was reported that the unit could seemingly withstand extensive thermal cycling without cracking or losing the bond with the embedded array of tubes [29,30].

The Masdar Institute in the UAE has researched a similar sensible heat storage concept for CSP plants. The concept, shown in Fig. 3, is a modular design that uses multiple thermal elements arranged in series and parallel. Each thermal element consists of a block of a special concrete (*Heatcrete VPI*) cast around a steel pipe. Several thermal elements are stacked inside a steel frame and are hydraulically connected through heat exchange piping [31].

An important difference between this design and the DLR's is that the pipes inside each element are configured so that the heat transfer fluid flows in and out of the element on the same side.

Two units with a capacity of 500 kWh<sub>th</sub> were built and approximately 300 charge and discharge cycles were carried out. A 100-kW electric heater was used to raise the temperature of the HTF (Dowtherm-A) up to 393 °C, which resembles the operating conditions of most commercial parabolic trough power plants.

It is reported that the measurements of the HTF's temperature after the units accumulated ~6000 h of cyclic operation demonstrate a stable and repetitive performance. Furthermore, a visual inspection of the

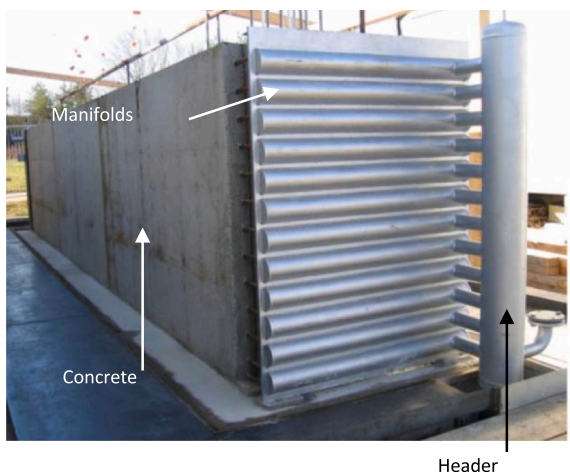


Fig. 2. DLR's concrete based TES unit.



Fig. 3. Masdar Institute's concrete-based modular heat storage system.

elements after ~6000 h of operation showed no degradation, cracking or separation between the steel pipes and the concrete [32].

## 3. An integrated thermal store and heat exchanger

As mentioned, this paper studies a concept for a directly charged high-temperature thermal energy store aimed at reducing the cost and footprint of CAES systems.

The integrated TES + HX unit consists of a non-pressurised container with approximately 29 tons of silica (desert) sand. An array of several straight stainless-steel pipes passes through the mass of sand and serves as the heat exchanger. The goal is to achieve a passive and very simple design that minimises fabrication costs. Fig. 4 shows a sketch of the concept for an integrated TES+ HX unit.

Silica sand has been studied as a heat storage and heat transfer material [33–40]. It has a high specific heat capacity, and it is readily available at low cost. Additionally, sand is a chemically inert material, which means that it will not react with any steel structure or air trapped inside the container.

Fig. 5 shows a schematic of the same high-temperature CAES system previously presented, but in here the TES and 3 intercoolers are replaced by the integrated TES + HX unit.

In this configuration, compressed air flows through the pipes of the TES + HX unit after emerging from the different stages of compression of the CAES system. Therefore, there will be three different pressure levels inside the unit. A third of the pipes will see a pressure of ~7 bar (stage

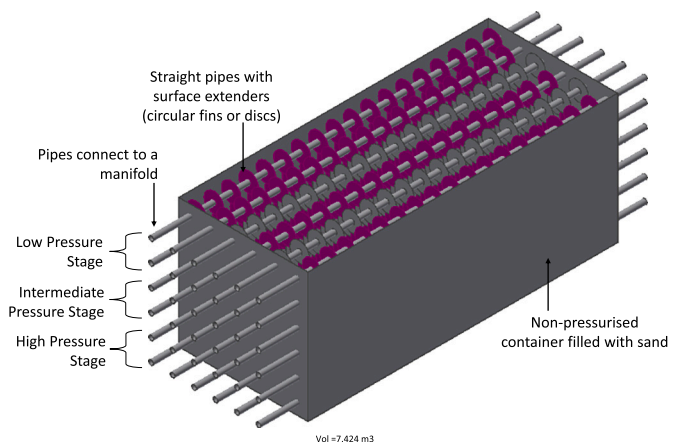


Fig. 4. Concept for an integrated TES + HX unit, intended to work within a CAES system.

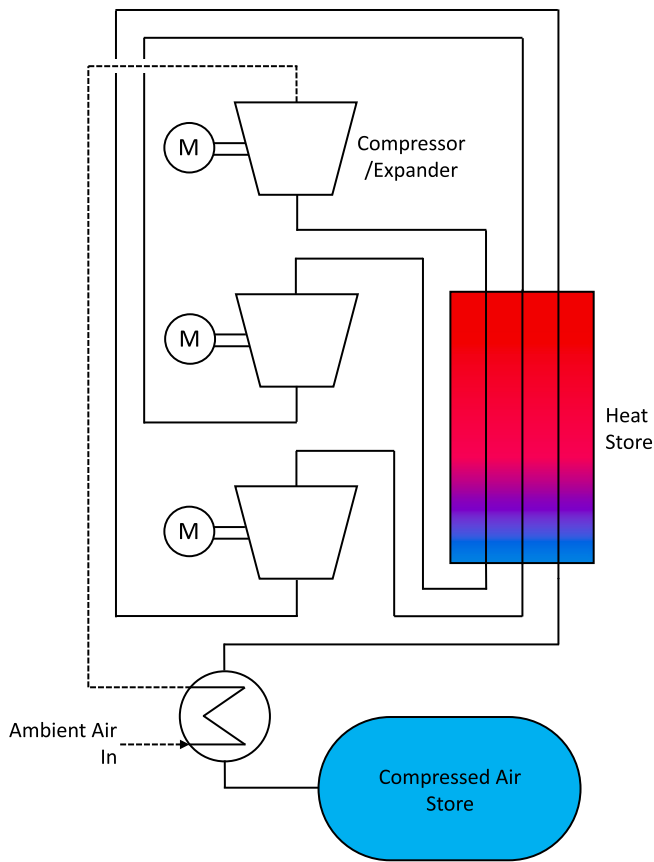


Fig. 5. A high temperature CAES system with a directly charged TES unit.

1), another third will see a pressure of ~40 bar (stage 2) while the remaining third of the pipes will hold a pressure of 250 bar (stage 3). Fig. 6 shows a side view of the unit to exemplify this.

As the expected diameter of the pipes is small (<20 mm), the savings that could be had by using pipes with different wall thicknesses for the 3 pressure levels are minimal. For simplicity, all the pipes are designed for the maximum pressure of 250 bar and have the same dimensions.

Every pipe in the unit has the same mass flow of air (albeit at different pressures) and the same inlet temperature. This allows having a single thermal front in the sand. On each side of the TES + HX unit, there will be three manifolds for the different pressure levels, to which the pipes will connect.

Similar to a packed bed of rocks, the integrated TES + HX will work as a thermocline. Inside the store there is a thermal gradient going from the inlet temperature (~550 °C) down to the outlet temperature (~214 °C). Packed beds where ambient pressure air flows inside the container are normally configured vertically to avoid any distortion of the thermal front caused by hot air in the container wanting to rise. However, in this integrated TES + HX unit compressed air is flowing through pipes, which makes possible to have a horizontal configuration.

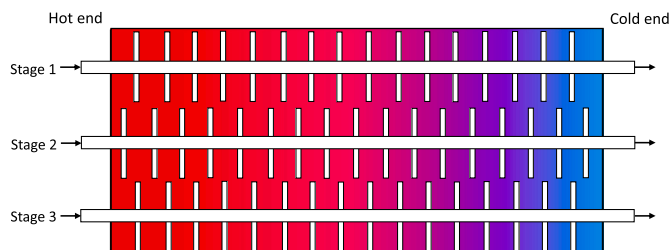


Fig. 6. Side view of integrated TES + HX unit operating in charge mode.

There are two main reasons for using sand instead of concrete. 1) Sand is cheaper and more readily available than a specially designed concrete mix. 2) To avoid potential cracks and poor contact between the pipes and the heat storage medium. Although such problems were not observed in [15–18] and [19,20], this is still considered a risk.

Sand can be poured around the pipes and it will accommodate the thermal expansion of the steel pipes while maintaining a good thermal contact, which is critical to achieving a good performance. A drawback of using sand is its poor thermal conductivity. To overcome this, the pipes have surface extenders in the form of discs or ‘fins’ (as shown in Figs. 4 and 6). These ‘finned tubes’ are commonly used in heat exchangers for the oil and gas industry.

The surface extenders or ‘discs’ present a techno-economical trade-off. The efficiency of the TES + HX unit will improve as the heat transfer area increases; however, this will also impact its cost. Modelling work will focus on finding the optimum balance between efficiency and cost.

Fig. 7 shows a diagram of the cross-section of the TES + HX unit. An array of 9 pipes is shown, although in reality there will be a few hundred of them. An important feature of the concept is that the pipes are arranged in a square grid. This configuration creates uniformity and symmetry inside the unit. Every pipe has the same amount of sand around it and the distance to other pipes is the same in every direction. This allows modelling the performance of the whole unit by analysing only a single pipe and the sand around it.

As it can be seen in Fig. 7, the diameter of the heat transfer discs is given by the unit’s width and the number of pipes. The discs cover almost all the cross-section of the TES + HX unit. An alternative is to have perforated plates through which the pipes pass. From a heat transfer point of view, both configurations are equivalent, but there may be differences in cost and ease of fabrication.

#### 4. Modelling

We use a two-dimensional transient model that simulates the charge and discharge of a particular design of a TES+ HX unit over a given work cycle. The model analyses a single pipe and the sand around it and uses those results to calculate the performance and cost-effectiveness of the complete unit.

The model calculates heat transfer between the air, steel pipe and sand in the radial and axial directions. Fig. 8 shows a side view of one

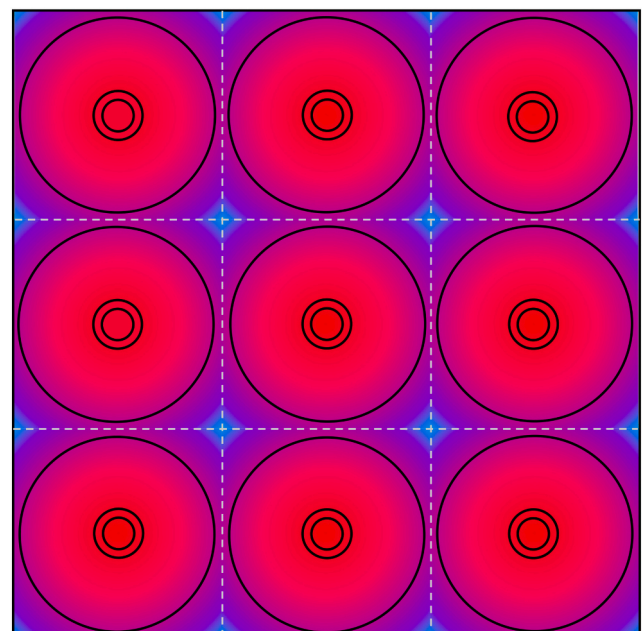


Fig. 7. Diagram of the cross-section of TES + HX unit.

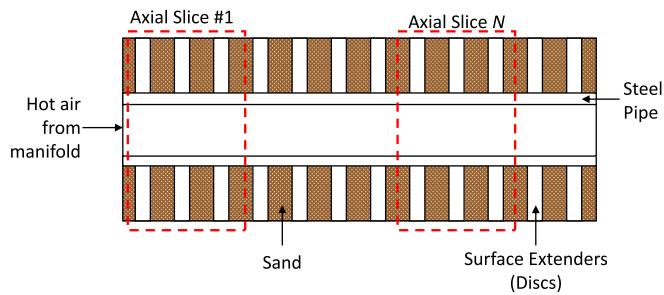


Fig. 8. Heat transfer pipe split into  $N$  elements or ‘slices’ along its longitudinal axis.

pipe surrounded by a mass of sand. The length of the pipe ( $L$ ) is divided into  $N$  axial elements or ‘slices’. Each slice comprises a segment of steel pipe, several heat-transfer discs, and some mass of sand.

The model uses a lumped approach. A bulk representation of the heat transfer discs in a slice is created by adding the mass and area of all the discs into a single element. The same is done for the sand.

Besides having a thermal gradient in the axial direction, inside each slice there is also a radial thermal gradient. To calculate the heat flows and track the radial temperature changes, the lumped masses of sand and discs are divided into radial elements or ‘rings’, as shown in Fig. 9.

Inside every axial slice, the model calculates the following heat flows: between the air and steel pipe, between the steel pipe and the 1st ring of sand, and between the steel pipe and the 1st ring of disc.

Then for each one of the radial elements in a slice, the model calculates: *i*) The heat flow between a ring of sand and the following, *ii*) the heat flow between a ring of heat-transfer disc and the following, *iii*) the heat flow between a ring of heat-transfer disc and the adjacent ring of sand.

The model also accounts for the advective heat transfer due to the air flowing from one slice into the next and some heat conduction from the sand and steel pipe in one slice to the next slice. These two heat flows creeping down the thermal front represent the ‘self-discharge’ of the

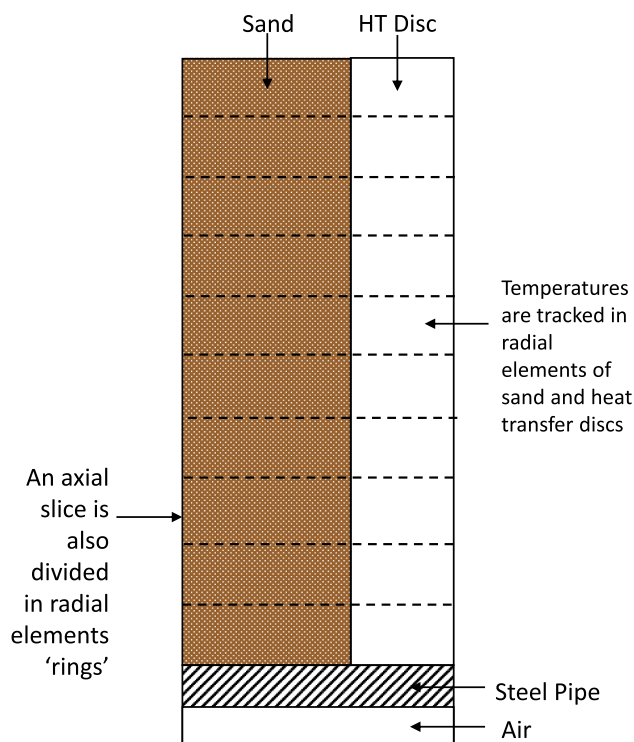


Fig. 9. Axial slice subdivided into  $n$  radial elements or ‘rings’.

unit.

The model considers the temperature dependency of the heat capacity and thermal conductivity of the three different materials involved: air, stainless steel and sand. The temperature dependency of the dynamic viscosity of the air is also accounted for. The stainless-steel properties have been taken from [41,42]. The properties of the sand used are from [33,43,44] while the air properties are provided by [45,46]. Fig. 10 provides plots of the thermal conductivities and specific heat capacities of the three materials.

It is important to mention that the model used in this paper has not been validated against experimental results. This model has been developed as an extension of the 1D model used and validated by the authors in previous work [47–49].

The work cycle considered consists of 8 h of charge at half power followed by 4 h of discharge at full power. This is representative of the duty that high-temperature CAES such as the one shown in Fig. 1 will serve. The pure storage phase between the charge and discharge is not modelled as self-discharge does not make a noticeable difference in a period of 12 h.

Several full work cycles (charge + discharge) are modelled until results converge. This ensures that the initial guess for the starting conditions of the unit does not affect the efficiency calculated. Convergence is reached when the state of charge (amount of exergy stored in the sand) of the unit at the start and end of a work cycle is the same.

During the 8-h charge cycle,  $\sim 1.020$  MWh of exergy are passed through the store. This figure comes from the 125 kW charge power of the CAES system. A part of this exergy is in the form heat, while another part is in the form of pressure. The TES + HX unit does not store any pressure, but it does incur pressure-exergy losses due to the pressure drop of the air flowing through the array of pipes.

The amount of heat-exergy ( $W_H$ ) that is put into the heat store during a charge cycle can be calculated by means of Eq. (1), where  $C_p$  is the specific heat of the air,  $\dot{m}$  is the total mass flow of air and  $T_0$  is ambient temperature. During a charge cycle, 567 kWh of heat-exergy are put into storage.

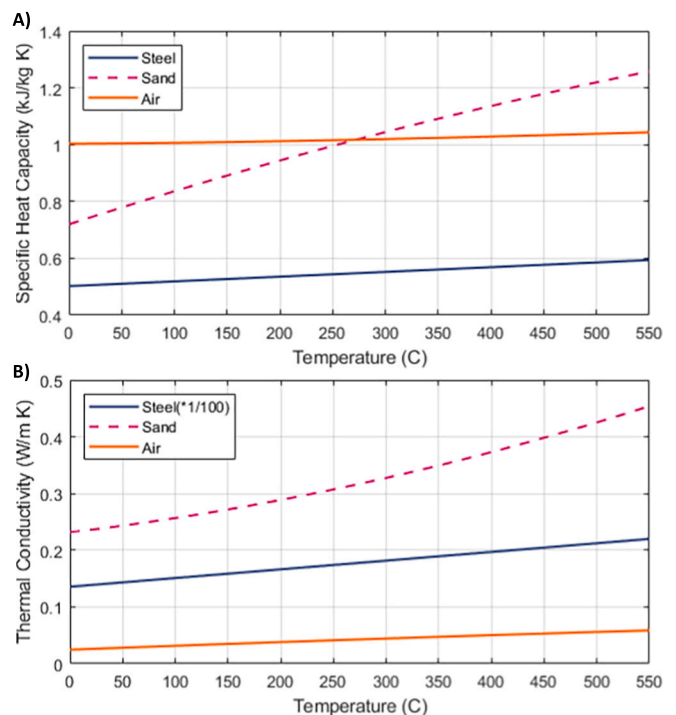


Fig. 10. Variation of the heat capacity (A) and thermal conductivity (B) of materials with respect to temperature.

$$WH = \dot{m}t \left( C_p \cdot \Delta T - T_0 \cdot C_p \cdot \ln \left( \frac{T_{in}}{T_0} \right) \right) \Bigg|_{T_{in}=214^\circ C}^{T_{in}=550^\circ C} \quad (1)$$

The total pressure-exergy ( $W_p$ ) that passes through the TES + HX unit during the charging period can be calculated through Eq. (2)

$$WP = \dot{m} \cdot t \cdot T_0 \cdot R_{air} \cdot \ln(r) \quad (2)$$

In Eq. (2),  $\dot{m}$  is the total mass flow of air passing through the TES + HX unit at any one time (equivalent to 3 times the mass flow through the CAES system's compression train),  $t$  is the duration of the charging phase (8 h),  $T_0$  is ambient temperature (20 °C) and  $r$  is the compression ratio of the CAES system (250<sup>1/3</sup>) Over the 8-hour charge cycle, 452 kWh of pressure exergy flow through the thermal store. This is evenly split between the three pressure levels.

The model accounts for four types of exergy loss: 1) exergy destruction due to heat transfer, 2) losses due to the air leaving the store with a  $T > 214$  °C (exhaust losses), 3) self-discharge losses and 4) exergy losses due to the pressure drop in the pipes. Heat losses to the environment are not considered.

Different designs will have different exergy losses. The roundtrip exergy efficiency of a unit accounts for all of these losses and can be calculated through Eq. (3)

$$\eta = \frac{A + B}{W_H + W_P} \quad (3)$$

In Eq. (3), **A** represents the heat-exergy content (above 214 °C) of the outlet air during the discharge cycle. This can also be calculated through Eq. (1), considering the appropriate mass flow of air during discharge, a discharge time of 4 h and the outlet temperature of the air.

In Eq. (3), **B** represents the pressure-exergy that is still available after losses during both, the charge and discharge cycles. The pressure-exergy losses during either cycle can be calculated as the difference between the inlet pressure-exergy and the outlet pressure-exergy of each one of the three streams of compressed air.

The outlet pressure-exergy ( $W_{P-out}$ ) for any one stage can be calculated by means of Eq. (4), where  $\dot{m}$  is the total mass flow of air,  $t$  is the duration of the cycle (8 h for charge, 4 h for discharge)  $P_{out}$  is the outlet pressure of the specific stream of air and  $P_{in}$  is the inlet pressure of that same stream.

$$W_{P-out} = \frac{\dot{m}}{3} \cdot t \cdot T_0 \cdot R_{air} \cdot \ln \left( \frac{P_{Out}}{P_{in}} \right) \quad (4)$$

The design of an integrated TES + HX unit presents a techno-economic trade-off. More expensive designs will tend to be more efficient, but in many cases the efficiency gains do not justify the increased cost. To compare between designs, an overall 'cost of storage' is used. This metric takes into consideration the cost of the store, the amount of exergy that can be discharged (recovered) and the cost of the exergy used to charge the store. The cost of storage is discussed in more detail in the following section.

### 5. Exploration of design space and optimisation

Using the thermal model described in Section 4, we analyse several different designs to identify the most cost-effective configuration. We study the effect of four design variables: the diameter of the pipes (OD), the spacing between heat transfer discs, the aspect ratio of the unit (AR) and an allowable fraction of pressure-exergy loss ( $\Omega$ ).

There are other variables such as the thickness of the discs that are fixed. In this case we fix this thickness to 1 mm, which is a value typically found in commercially available finned pipes.

The mass of sand is also fixed at 29 tons. This is given by the heat storage capacity required for the CAES system. To store 1 MWh of heat in the temperature range between 214 °C and 550 °C we need a minimum

of 9.7 tons of sand. As a rule of thumb, packed beds use a mass over-rating factor between 2 and 3 to improve the storage efficiency. We use a factor of 3.

Fig. 11 shows a flowchart that illustrates how the exploration of the design space is carried out.

We explore three different pipe diameters: 7 mm, 10 mm and 20 mm. For each one we evaluate three different disc spacings: 5 mm, 15 mm and 60 mm. For each combination of pipe OD and disc spacing we analyse several combinations of aspect ratio (length/width) and fraction of pressure exergy loss ( $\Omega$ ). The aspect ratio has a range between 5 and

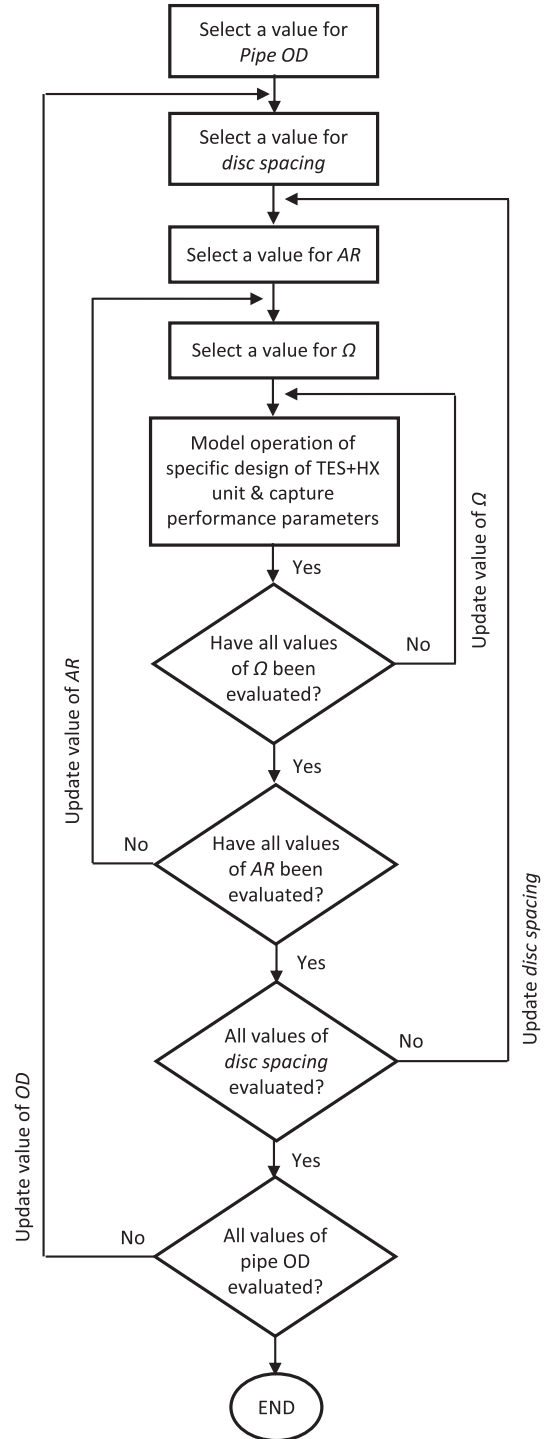


Fig. 11. Exploration of design space: pipe OD, disc spacing, aspect ratio (AR) and fraction of pressure exergy loss ( $\Omega$ ).

12, while  $\Omega$  goes from 0.001 to 0.08.

The wall thickness of the pipes is calculated via Eq. (5) based on the strength of the steel ( $S = 100$  Mpa) and the maximum pressure they will hold. For ease of fabrication, all pipes are designed for the same maximum pressure of 250 bar.

$$\text{Wall Thick}_{\min} = \frac{OD_{\text{pipe}} \cdot P_{\max}}{2 \cdot S} \quad (5)$$

After calculating the minimum wall thickness required, a small corrosion allowance is added to the OD. The thickness of the heat transfer discs is set to 1 mm, which is a typical value in commercially available finned tubes.

The diameter of the heat transfer discs is given by the width of the unit's cross section divided by square root of the total number of pipes, as shown in Fig. 8. Because the mass and volume of sand is constant across all designs, the aspect ratio sets the dimensions of the container. The pipes have the same length as the container.

The allowable fraction of pressure exergy loss ( $\Omega$ ) is a fraction of the total pressure-exergy that is passed through the store during the charging phase ( $W_p$ ), which can be calculated through Eq. (2). The allowable loss of pressure exergy encompasses losses during both, the charge and discharge phases.

The number of pipes in the unit is calculated so that the roundtrip pressure exergy losses across all three pressure stages do not exceed the defined allowable level. This is an iterative calculation. We start by making an initial guess for how many pipes there are in the unit. Each of those pipes sees the same air mass flow. Then, for each of the three pressure levels we calculate a pressure drop during both, the charge and discharge phases, which can be done through Eqs. (6) to (12).

Because the temperature gradient inside the unit is not yet known, we assume an air temperature equal to the temperature of the hot side ( $T_{\max} = 550^\circ\text{C}$ ). In the equations  $v$  is the velocity of the air flow,  $\dot{m}$  is the total mass flow through the TES + HX unit (0.73 kg/s during discharge),  $\rho$  is the density of the air,  $Re$  is the Reynolds number,  $\mu$  is dynamic viscosity of the air,  $Pr$  is the Prandtl number,  $Nu$  is the Nusselt number,  $f$  is a friction factor and  $\Delta P$  is the pressure drop throughout the length of a pipe.

$$\rho = \text{Stage Pressure} \cdot (R_{\text{air}} \cdot T_{\max})^{-1} \quad (6)$$

$$v = \frac{\dot{m}}{No\ Pipes} \cdot (\rho \cdot \text{flow}_{\text{area}})^{-1} \quad (7)$$

$$Re = \rho \cdot v \cdot ID_{\text{pipe}} \cdot \left(\frac{1}{\mu}\right) \quad (8)$$

$$Nu = 0.023 \cdot Re^{0.8} \cdot Pr^{0.33} \quad (9)$$

$$\phi = -1.8 \cdot \log \quad (10)$$

$$f = \left(\frac{1}{\phi}\right)^2 \quad (11)$$

$$\Delta P = \frac{f \cdot \rho \cdot v^2 \cdot \text{PipeLength}}{2 \cdot ID_{\text{pipe}}} \quad (12)$$

After knowing the pressure drop for each one of the 3 pressure levels during the charge and discharge processes, we can calculate the associated loss of pressure exergy by means of Eq. (4). If this is greater than the allowable value, then the guess for the number of pipes in the unit is increased.

The 'levelized cost of storage' ( $LCoS$ ) is used to compare different designs. This metric considers the capex of the unit, its efficiency and the cost of the energy used to charge it. The  $LCoS$  of a TES + HX unit can be calculated via Eq. (13), where  $x$  is a discount rate of 5 % and  $\lambda$  is the lifetime of the unit, which is considered to be 25 years

$$LCoS = \frac{\text{Capex} + \sum_{i=1}^{\lambda} \frac{\text{Chargingcost}}{(1+x)^i}}{\text{Exergy discharged over Lifetime}} \quad (13)$$

The capex of the store considers the cost of the steel used ( $\alpha$ ), the cost of welding the array of pipes to manifolds on both sides ( $\beta$ ) and the cost of inspection those welds through x-rays ( $\gamma$ ), as Eqs. (14)–(17) show.

$$\text{Capex} = \text{Cost}_{\text{Steel}} + \text{Cost}_{\text{welding}} + \text{Cost}_{\text{xray}} \quad (14)$$

$$\text{Cost}_{\text{Steel}} = \alpha \cdot \text{Mass}_{\text{Steel}} \quad (15)$$

$$\text{Cost}_{\text{welding}} = \beta \cdot \pi \cdot OD \cdot 2NoPipes \quad (16)$$

$$\text{Cost}_{\text{xray}} = (\gamma \cdot 2NoPipes) \quad (17)$$

In this study we assume a cost of 4 £/kg for 'processed' steel ( $\alpha$ ), a cost of 0.5 £/mm for welding the pipes to a manifold ( $\beta$ ) and an x-ray inspection cost of £10 per joint ( $\gamma$ ). A lifetime ( $\lambda$ ) of 25 years is considered with 1 full charge + discharge cycle per day. The system takes in 1MWh during a charging phase; the cost per kWh of electricity considered is 0.05 [50]. The amount of exergy discharged over the lifetime of the system takes into account both, the heat-exergy and the pressure-exergy that emerge from a TES + HX unit every discharge cycle.

## 6. Analysis of results and discussion

### 6.1. Pipe OD of 10 mm and disc-spacing of 15 mm

In this section we focus on a pipe OD of 10 mm and a spacing between heat transfer discs of 15 mm. For these values, Fig. 12 shows the effect that variations in the aspect ratio and the fraction of allowable pressure exergy loss have on the  $LCoS$  of the integrated TES + HX unit.

These two parameters control a trade-off between exergy efficiency and capital cost. We discover that designs based on small values of  $\Omega$  achieve high exergy efficiencies but have a high cost too, whereas designs based on large  $\Omega$  values sacrifice some efficiency for the sake of a lower capital cost. We can see in Fig. 12 that for each AR there is an optimum value of  $\Omega$  that minimises the levelized cost of the unit. The minimum  $LCoS$  is 35.08 £/MWh, which is achieved by a unit based on an AR of 12 and an  $\Omega$  of 0.01.

As we move to smaller values of  $\Omega$  the number of pipes in the array increases quite significantly in order to minimise the mass flow of air per pipe and consequently the pressure drops seen. The OD and wall

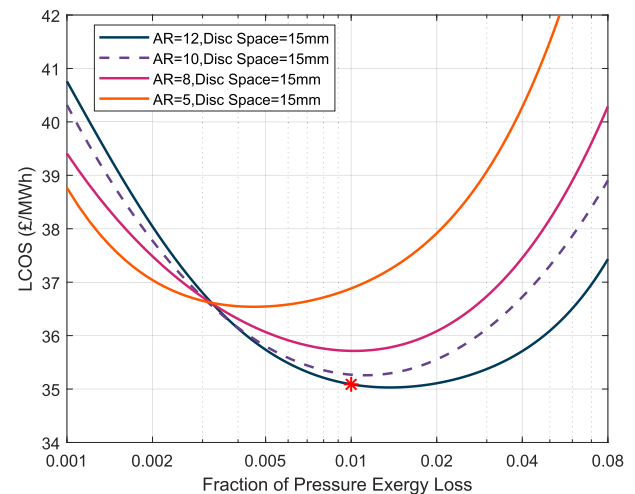


Fig. 12. Effect of aspect ratio (AR) and fraction of pressure exergy loss ( $\Omega$ ) on the cost of storage. Pipe OD and disc spacing are fixed to 10 mm and 15 mm, respectively.

thickness remain constant. For example a unit with an AR of 10 will require some 1089 pipes to achieve a pressure exergy loss of 0.1 % of the total input while it only requires 100 pipes for a  $\Omega$  of 8 %. For any given  $\Omega$ , the number of pipes is directly proportional to the aspect ratio. If the length of the pipes increases, more pipes are needed to maintain pressure drops below the specified level.

Fig. 13 shows the roundtrip exergy efficiency achieved by designs based on different combinations of AR and  $\Omega$ . Designs based on small  $\Omega$  values achieve high efficiencies for two reasons: i) exergy losses due to pressure drops are small and ii) there is considerably more heat transfer area due to the greater number of pipes. Regardless of the aspect ratio, designs based on a  $\Omega$  of 0.001 have ~10 times more surface area than designs for a  $\Omega$  of 0.08.

We can also see in Fig. 13 that the roundtrip exergy efficiency of a TES + HX unit improves as its aspect ratio increases. This is because the steel-sand heat transfer area is directly proportional to AR. There are 2 reasons for this: 1) the surface area of each pipe increases with length and 2) more pipes are used in the array. For reference, designs based on an aspect ratio of 12 will have ~2.5x more pipe surface area (regardless of  $\Omega$ ) than designs based on an AR of 5.

The surface area provided by the heat transfer discs reduces slightly as the aspect ratio of the unit increases. In principle this should remain constant; however, more pipes of the same OD are used as AR increases, so a larger fraction of the unit's cross section is occupied by the pipes' void centres. This reduction in the surface area is small compared to the total heat transfer area that the discs provide.

Fig. 14(A) shows how the total heat transfer area of a TES + HX unit varies with respect to its aspect ratio and the allowable fraction of pressure exergy loss ( $\Omega$ ). We can see that the overall heat transfer area is directly proportional to AR and inversely proportional to the value of  $\Omega$ . As a greater pressure drop is allowed fewer pipes are required in the array, which reduces the available heat transfer area.

In Fig. 14(B) we can see the contribution of the discs to the total heat transfer area of the unit. There are two conditions that entail an increased number of pipes in the array: a greater AR and a small  $\Omega$ . In these situations, the pipes contribute more to the overall heat transfer area and the contribution of the discs is reduced.

Fig. 15 shows how the total mass of steel used for the construction of a TES + HX unit changes with respect to the aspect ratio and  $\Omega$ . For any given AR, the mass of steel increases as  $\Omega$  reduces because more pipes are being used. The mass of discs varies between 3600 and 4200 kg, which is a relatively narrow range. The mass of steel is an important contributor to the capital cost of a TES + HX unit.

Fig. 16(A) shows the effect of the aspect ratio and the fraction of allowable pressure exergy loss on the capital cost (capex) of the heat

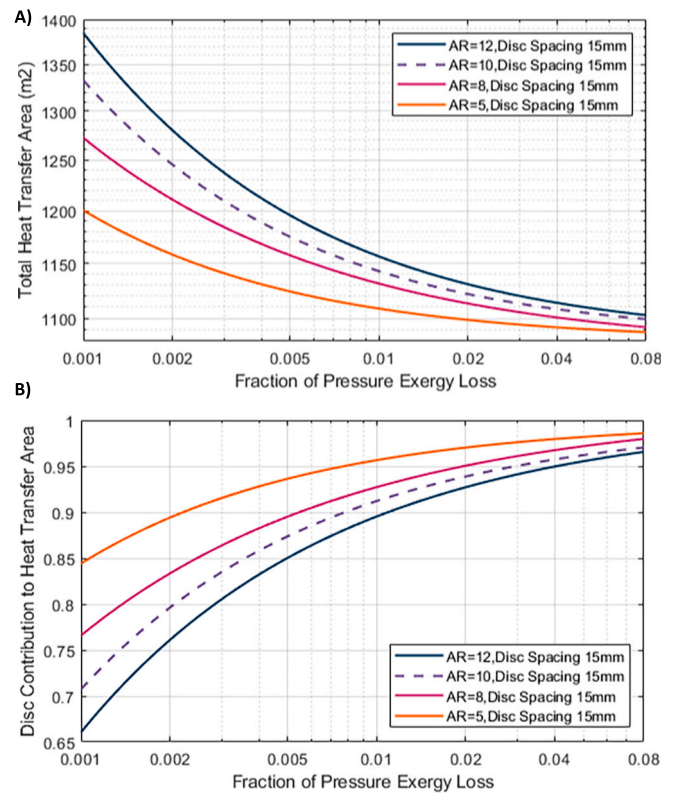


Fig. 14. A) Total heat transfer area achieved by different designs. Pipe OD = 10 mm, disc spacing = 15 mm. B) Contribution of discs to total surface area.

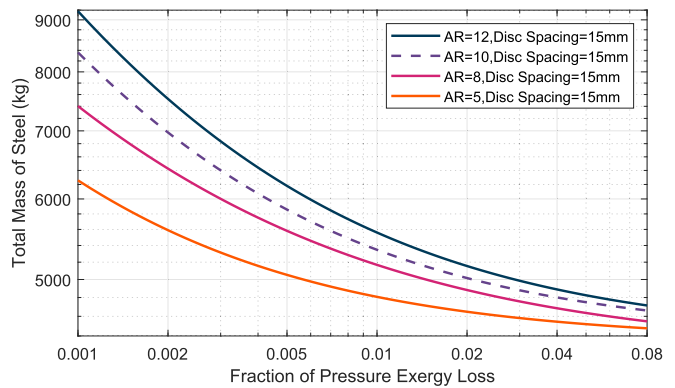


Fig. 15. Total mass of steel used by different TES + HX designs. Pipe OD and disc spacing are constant.

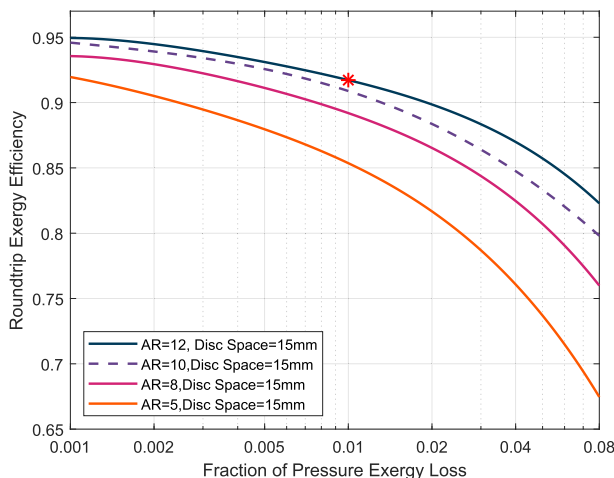


Fig. 13. Roundtrip exergy efficiencies achieved by different designs (pipe OD = 10 mm, disc spacing = 15 mm).

store. The capex is directly proportional to AR and inversely proportional to  $\Omega$ . Both relationships are linked to the number of pipes in the array. A greater number of pipes translates into a larger mass of steel, but it also represents increased welding and x-ray costs. Put simply, the more efficient a design is the more expensive it will be (see Fig. 13).

Focusing on an aspect ratio of 12, Fig. 16(B) provides a breakdown of the capex. At large values of  $\Omega$ , the cost of steel dominates the total cost because the reduced number of pipes lowers the welding and x-ray costs. On the other hand, at small values of  $\Omega$ , the cost of welding the pipes to the inlet and outlet manifolds can represent up to 40 % of the total capex of the unit.

Going back to Fig. 13, we can see that for a pipe OD of 10 mm and a disc spacing of 15 mm, the most efficient design is found with an  $\Omega$  of 0.001 and an AR of 12. This configuration achieves a roundtrip exergy efficiency of 94.9 % and a levelized cost of storage of 40.76 £/MWh.

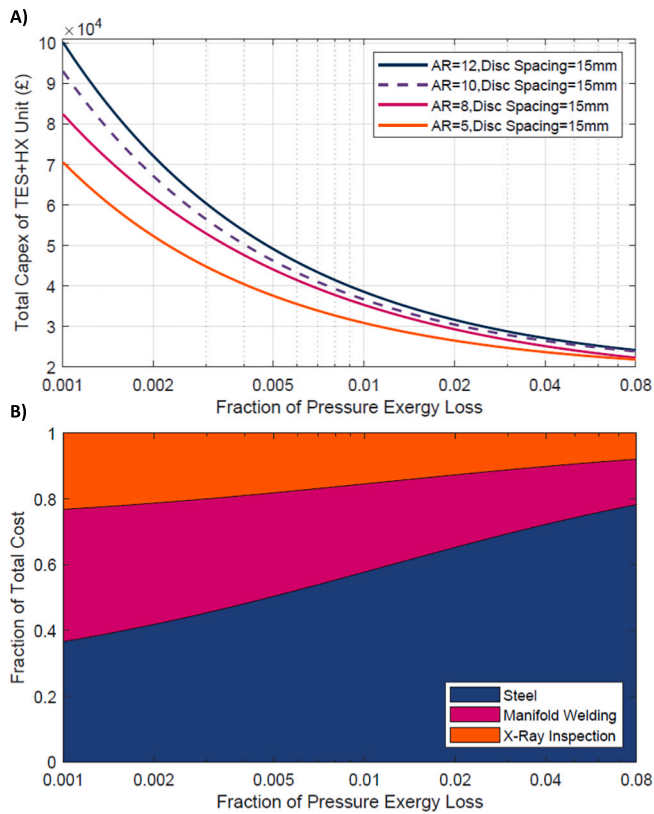


Fig. 16. A) Total capital cost achieved by different TES + HX designs. Pipe OD = 10 mm and disc spacing = 15 mm. B) Breakdown of the capex a unit with an aspect ratio of 12.

However, the most cost-effective design (i.e. lowest  $LCoS$ ) is achieved with a pressure exergy loss of  $\sim 0.01$  and an AR of 12. This design has a capex of  $\sim £38.5k$  and achieves an efficiency of 91.8 %, which translates into a  $LCoS$  of 35.08 £/MWh. This TES+ HX unit has a length of 11.65 m, a width of 0.97 m and uses 289 straight pipes. The capex of this design is only a small fraction ( $\sim 26$  %) of the cost of the ‘heat storage subsystem’ (packed bed and 3 heat exchangers) of a CAES system. Section 6.4 provides a broader discussion on this point.

Fig. 12 suggests that increasing the aspect ratio further will result in a lower  $LCoS$ . A value of 12 was set as the upper limit as longer units are impractical due to their footprint. A hairpin configuration may be used; however, that could significantly increase the capex of the unit due to a greater number of welded joints.

Fig. 17 shows the temperature gradients seen by different designs after the unit completes a full work cycle (8 h charge, + 4 h discharge). As mentioned in Section 4, the heat transfer model analyses a single pipe and the sand surrounding it. The performance of the complete unit is estimated based on the single pipe results.

In the plots, the x-axis represents the axial position within the unit, with 0 being the ‘hot end’ and 1 being the ‘cold end’. The figures show the temperature profiles of air and sand at the start and at the end of a charging cycle. Besides the temperature gradient in the axial direction, there is also a radial gradient (away from the pipe). The sand immediately next to the pipe’s wall is hotter than the sand farthest away from it. The plots in Fig. 17 show the temperature of the sand element that is furthest away from the pipe.

Fig. 17 compares designs based on two aspect ratios (8 and 12) and different values of  $\Omega$  (0.002, 0.005 and 0.01). We can see that for a given AR, the temperature profiles improve as the value of  $\Omega$  reduces. This is largely due to the increased number of pipes and available heat transfer area.

Towards the end of a charge cycle, the temperature of the cold end

increases which causes air to emerge from the unit at a temperature higher than nominal. This is a loss of exergy (exhaust losses) and has a strong two-fold impact on the efficiency of the unit. During the subsequent discharge, air at the nominal ‘cold’ temperature will enter the unit through the cold side and encounter a much higher temperature in the sand and steel pipes. This inevitably destroys exergy.

The temperature increase of the cold side worsens as  $\Omega$  increases. For example, a TES + HX unit based on an AR of 8 and  $\Omega = 0.002$  will see a cold end temperature approximately 63° higher than nominal at the end of a charge cycle. When the value of  $\Omega$  increases to 0.01 this delta increases to 74 °C.

Interestingly, these same values apply for the hot side too. At the end of a discharge cycle the temperature of the hot side of the unit will be lower than the nominal value. At the end of a discharge, the hot side of a unit based on an AR of 8 and a  $\Omega$  of 0.01 will be 74 °C lower than nominal.

Minimising the reduction in the temperature of the hot end is important as it has an impact on the expanders downstream of the TES + HX unit. The isentropic efficiency of an expander is very sensitive to the temperature of the incoming gas. Ideally, an expander will be optimised for a single and constant inlet temperature. Expanders can also be well tuned to operate over a small range of inlet temperatures without a significant loss of efficiency. However, if the range of inlet temperatures is broad, the expander will operate sub-optimally for a part of that range, which will hurt the efficiency of the CAES system.

The outlet temperature profile of a packed bed during a discharge cycle is different to that of a TES + HX unit. A packed bed can provide an almost constant temperature for a great part of the discharge cycle. This is owed to their very large heat transfer area which is achieved by the direct contact between the air and the rock pebbles. Towards the end of the cycle, the outlet temperature reduces as the packed bed loses charge. A packed bed sized for the same duty as the TES + HX unit might see a temperature reduction of  $\sim 30$  °C in its outlet temperature.

The outlet temperature of a TES + HX unit reduces gradually from the beginning of a discharge cycle. If this temperature drop is kept to a relatively small value ( $\sim 60$  °C or less), the expander downstream can still operate efficiently. This is an important consideration while ‘optimising’ the design of a TES + HX unit.

Regardless of the type of heat store used, either a TES + HX unit or a packed bed, an electric heater (or solar thermal collector) can be included in the CAES system to ‘top-up’ or boost the outlet temperature of the heat store. This adds cost to the system but can improve the discharge efficiency. Exploring this further is out of scope for this paper as it is a ‘whole CAES system’ decision.

We can also see in Fig. 17 that the temperature difference between the sand and the air grows as the value of  $\Omega$  increases. Focusing on an AR of 12, a TES + HX unit based on a value of  $\Omega$  of 0.002 has a mean temperature difference between the sand and the air of  $\sim 8.9^\circ$ . This is measured across the complete length of the thermal gradient at the end of a charge cycle. The mean temperature difference increases to 14° for a  $\Omega$  of 0.01. This difference between the temperature profiles of air and sand are a few degrees more pronounced at the end of a discharge cycle.

Another important phenomenon revealed by the plots in Fig. 17 is the separation between the temperature profile of the sand elements at the start and at the end of a charging cycle. We measure this delta in three places along the profiles (at axial locations 0.2, 0.5 and 0.8). A design based on an AR of 12 and a  $\Omega$  of 0.01 sees a temperature difference of approximately 43°, which increases to  $\sim 72^\circ$  when  $\Omega$  reduces to 0.002. This indicates that more heat is being stored in the sand, which means that less heat-exergy is being destroyed or lost in the form of exhaust losses.

Fig. 17 has established that the temperature profiles deteriorate as the allowable fraction of pressure-exergy loss increases. We can also see that for any given value of  $\Omega$ , the profiles worsen as the AR reduces. These observations support the conclusion drawn from Fig. 13, which is that the roundtrip exergy efficiency of a TES + HX unit is directly

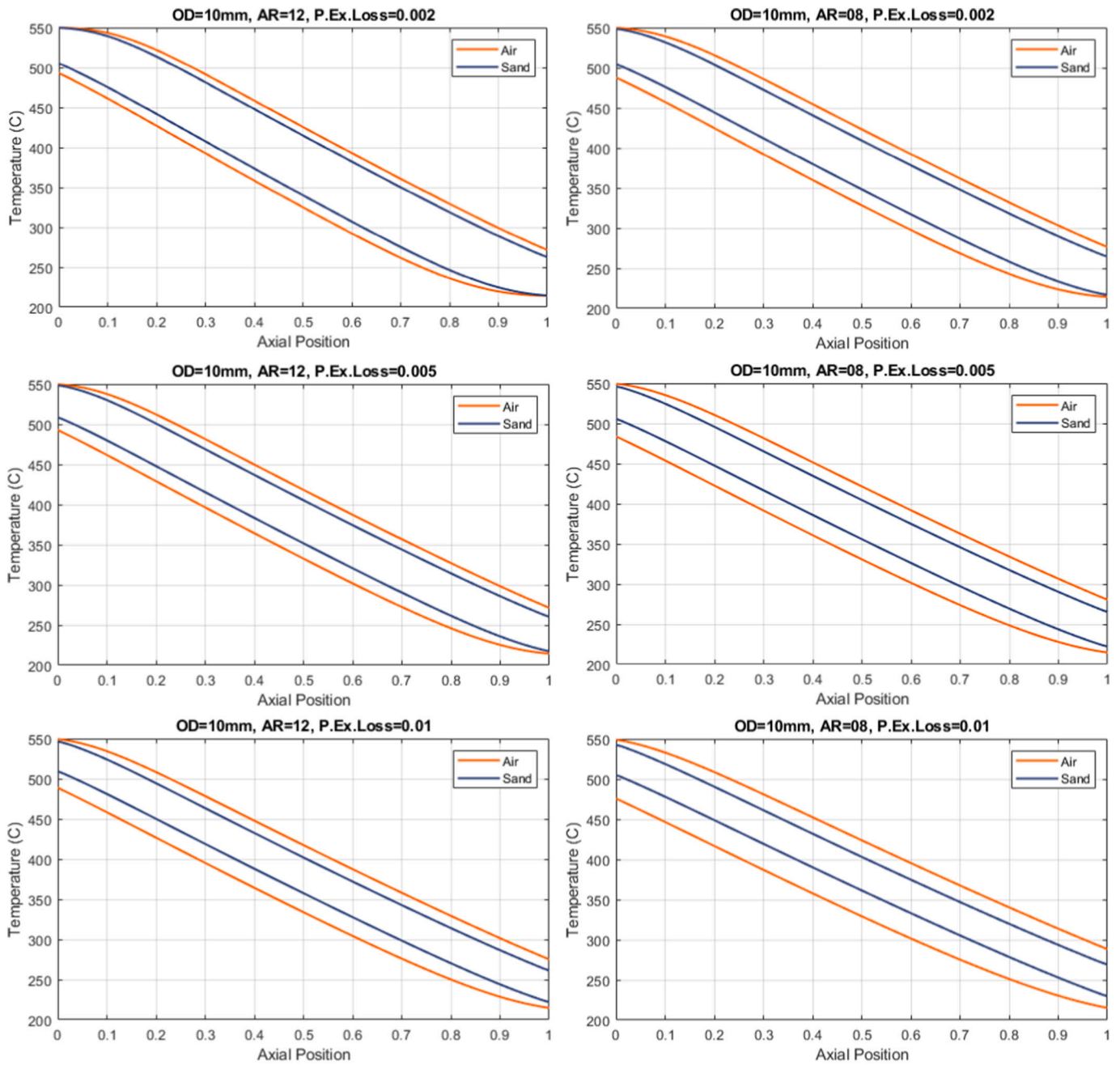


Fig. 17. Temperature gradients seen by designs based on different aspect ratios and fractions of pressure exergy loss. Pipe OD = 10 mm and disc spacing = 15 mm.

proportional to the aspect ratio and inversely proportional to the value of  $\Omega$ .

6.2. Effect of varying the disc spacing

This section explores the effect of varying the spacing between heat transfer discs while keeping the pipe OD constant at 10 mm. We have established that the efficiency of a TES + HX unit depends largely on the available heat transfer area. Varying the spacing between discs will change the available heat transfer area but it will also affect the cost of the unit.

Fig. 18 shows the levelized costs of storage achieved by different heat store designs, considering a reduced disc spacing of 5 mm (top) and an increased disc spacing of 60 mm (bottom). The red horizontal line at 35.08 £/MWh indicates the LCoS attained by the most cost-effective configuration with a disc spacing of 15 mm (previously shown in

Fig. 12).

It is clear that in both cases, a reduced and an increased disc spacing, the levelized costs of the different units are higher than what is achievable with a spacing of 15 mm. The lowest LCoS seen with a disc spacing of 5 mm is 37.4 £/MWh and is achieved by a unit with an AR of 12 and an  $\Omega$  of 0.018. On the other hand, considering a disc spacing of 60 mm, a design based on an aspect ratio of 12 and an  $\Omega$  of 0.008 achieves a LCoS of 35.45 £/MWh.

The increase in LCoS caused by increasing the spacing between discs from 15 mm to 60 mm is relatively small compared to the increase seen when the spacing is reduced to 5 mm. This suggests that the capital cost has a stronger effect on the LCoS than the exergy savings.

The fact that both, an increase and a reduction in the disc spacing with respect to the reference value of 15 mm causes an increase in the LCoS suggests that a spacing of 15 mm is a near-optimal value. Due to how computationally expensive each analysis is, we cannot determine

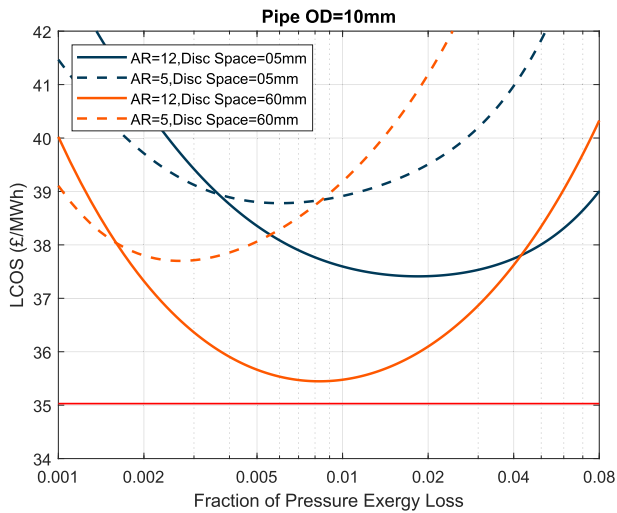


Fig. 18. Effect of the levelized cost of storage of varying the spacing between heat transfer discs.

more accurately the true optimum value for the disc spacing.

Fig. 19 shows how the spacing between heat transfer discs affects the roundtrip exergy efficiency of a TES + HX unit. The same general behaviour discussed in Section 6.1 can be seen in the figure. Designs based on small  $\Omega$  values and larger aspect ratios achieve higher efficiencies due to an increased heat transfer area resulting from a greater number of pipes. For any given value of AR and  $\Omega$ , a narrower disc spacing leads to a higher efficiency, as having more discs in a given length increases the total steel-sand contact area.

The improvement in efficiency obtained from a reduced spacing is not so noticeable in designs that already have a high efficiency due to a small  $\Omega$  value or a large AR. In those situations: 1) the pipes already provide a significant amount of surface area and 2) the distance between pipe centres shortens, which reduces the distance that heat travels across the sand and limits the benefit provided by the heat transfer ‘enhancement’ discs. The most efficient design using a disc spacing of 5 mm achieves a roundtrip exergy efficiency of 95.8 %. This is only marginally better than the 94.9 % achieved with a spacing of 15 mm (see Fig. 13).

The improvement in efficiency due to a reduced disc spacing is most noticeable when the available heat transfer area is small and when the distance from a pipe to the sand furthest away from it is long (e.g. small AR). For example, a design based on an AR = 5, an  $\Omega$  of 0.04 and 15 mm of disc spacing achieves an efficiency of 76 %, while if the spacing is

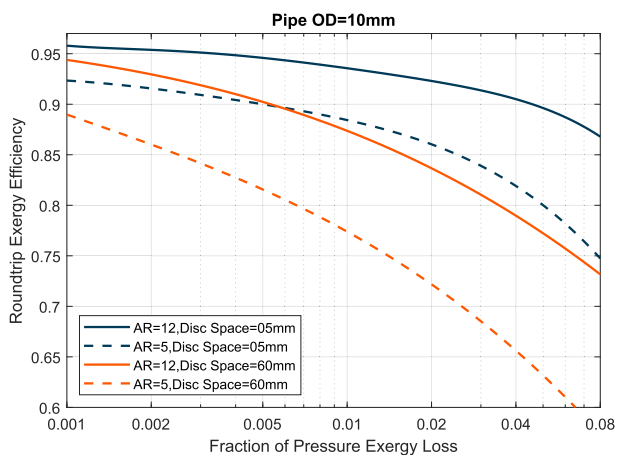


Fig. 19. Effect that varying the disc spacing has on the exergy efficiency of the TES + HX unit.

reduced to 5 mm, its efficiency increases to ~82 %.

Fig. 20 shows effect that varying the spacing between heat transfer discs has on the total available surface area of the unit. The area provided by the pipes in the array is independent from the disc spacing; however, it changes with respect to AR and  $\Omega$ .

As we change the spacing between heat transfer discs, the area provided by them changes by a factor ( $z$ ), as Eq. (18) shows, where  $d$  is the thickness of the discs. As mentioned in Section 5, we have set this to be 1 mm. For example, reducing the spacing from 15 to 5 mm will increase the surface area provided by discs by a factor of 2.66.

$$z = \frac{d + spacing_1}{d + spacing_2} \tag{18}$$

Fig. 21 shows how the total mass of steel varies with respect to the aspect ratio,  $\Omega$  and disc spacing. The OD of the pipes is still fixed at 10 mm, so the only difference between this figure and Fig. 15 is the amount of discs in the array.

As previously established, the mass of steel used for the unit is directly proportional to AR and inversely proportional to  $\Omega$  because more pipes (of the same OD) are used in the array. We can see that reducing the spacing between discs to 5 mm has a marked effect on the mass of steel.

For example, a design based on an AR of 12 will see an increase of between 1.66 $\times$  and 2.5 $\times$  in the mass of steel used, depending on the value of  $\Omega$ . On the other hand, increasing the spacing between discs from 15 mm to 60 mm (with an AR = 12) will cause a reduction in the steel mass by a factor of 0.33–0.7, depending on the value of  $\Omega$ .

Fig. 22 shows how the capital cost of a TES + HX unit varies with respect to the spacing between discs. The same general behaviour can still be seen, designs based on small  $\Omega$  and large aspect ratios have higher costs due to the larger number of pipes required.

A tighter spacing between heat transfer discs increases the capital

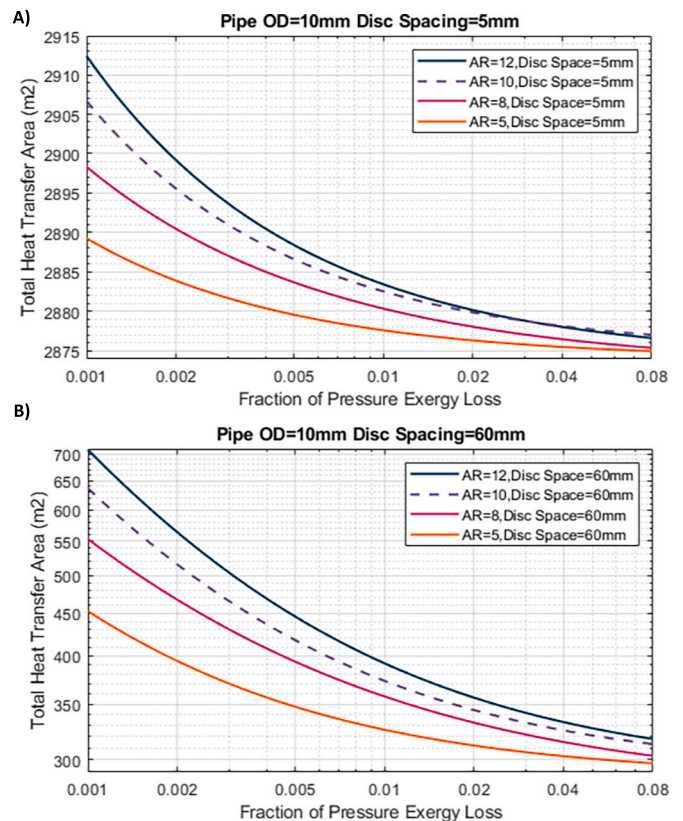


Fig. 20. Variation in the total heat transfer area with respect to disc spacing. A) Spacing = 5 mm, B) spacing = 60 mm.

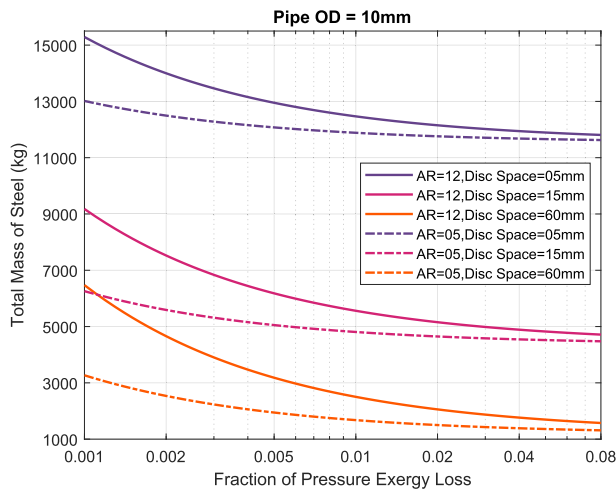


Fig. 21. Total mass of steel used in different designs. All designs consider a pipe OD = 10 mm.

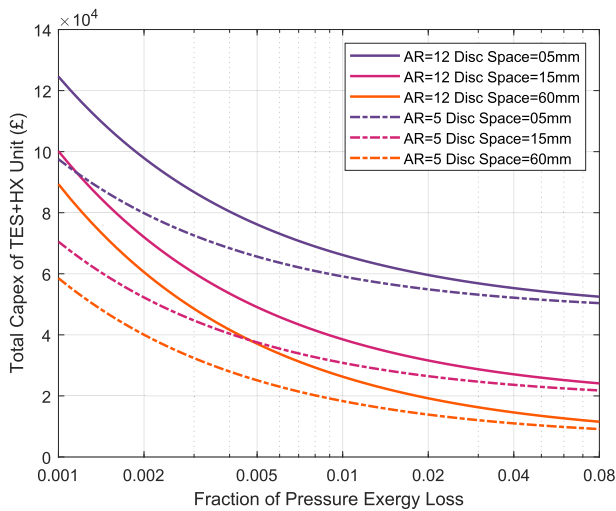


Fig. 22. Effect that varying the disc spacing has on the capital cost of a TES + HX unit.

cost, while a wider gap between discs reduces the cost. For example, for an AR of 12 and a fraction of pressure exergy loss of 0.01, reducing the disc spacing from 15 mm down to 5 mm increases the capex by a factor of ~1.7. Conversely, increasing the disc spacing from 15 mm to 60 mm reduces the capex of the unit by a factor of ~0.68.

The increased capex owed to a reduced disc spacing overshadows the efficiency gains obtained (see Fig. 18). Similarly, the savings in capital cost from a wider spacing between discs do not compensate for the additional cost of the lost exergy.

Fig. 23 shows the effect that the spacing of heat transfer discs has on the thermal gradient of a TES + HX unit. All plots show a design based on an AR of 12 and an  $\Omega$  of 0.005. We can clearly see that the temperature profiles worsen as the spacing between discs increases from 5 mm to 60 mm.

A way to quantify this is measuring the mean difference between the temperature profiles of the sand (furthest away from the pipe) and the air. This difference is calculated as the average difference between the two curves through the complete axial length of the unit. When the spacing between discs is 5 mm, this mean difference is ~9.8°. The difference increases to 14.4° for a spacing of 60 mm between discs.

Another criterion to evaluate the thermal gradient is to measure the temperature of the cold end of the unit at the end of a charge cycle. For

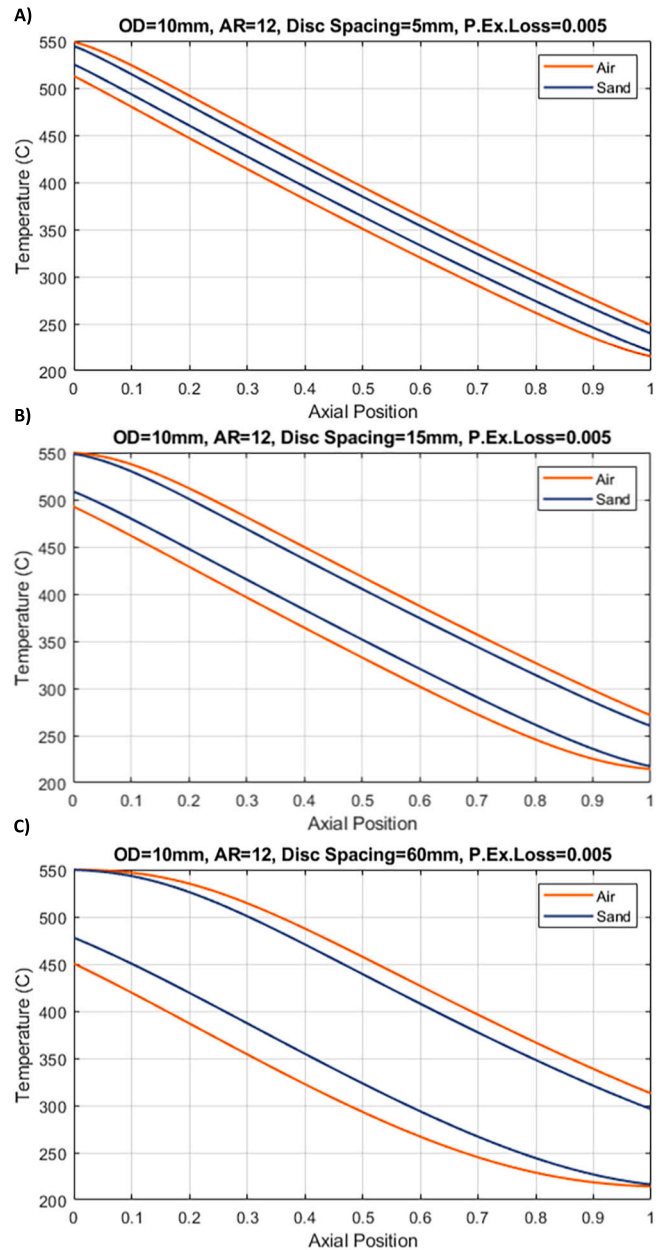


Fig. 23. Thermal gradients seen by TES + HX units with various disc spacings. A) = 5 mm, B) = 15 mm, C) = 60 mm. Pipe OD (10 mm), AR (12), and  $\Omega$  (0.005) are constant.

the CAES system considered in this study, the nominal ‘cold’ temperature is 214 °C (see Sections 1 and 3). The cold end of a TES + HX unit with based on an AR of 12 and an  $\Omega$  of 0.005 reaches 248.7 °C at the end a charge (Fig. 25a), which is 34.7 °C higher than the nominal value. For comparison, this delta increases to 57.5 °C for a disc spacing of 15 mm and to 98.7 °C when discs are separated 60 mm.

As discussed in Section 6.1, a rise in the temperature of the cold end of a TES + HX unit creates further exergy losses during the subsequent discharge cycle due to the temperature difference between the inlet air and the sand.

During the following discharge cycle, the temperature of the unit’s hot end (i.e. outlet temperature) will reduce from its nominal temperature of 550 °C. The temperature drop of each one of the 3 designs (disc spacing of 5 mm, 15 mm and 60 mm) is very similar to the delta observed at the cold side during charge. For example, the hot end of a unit considering a disc spacing of 60 mm will see a temperature drop of

~99 °C at the end of the discharge.

Fig. 24 shows how the temperatures of the hot (A) and cold (B) ends of three TES + HX units considering different disc spacings evolve throughout a work cycle. During the charge cycle (first 8 h), the hot ends of the 3 designs almost reach the nominal temperature. The unit with a disc spacing of 60 mm reaches a slightly higher temperature than the other two thanks to its smaller steel mass. However, this difference is small (<5 °C).

During the discharge cycle (last 4 h), a unit with a 5 mm disc spacing maintains a higher temperature at its hot end compared to the other two designs with wider spacings. This is owed to the fact that it has more surface area which enables it to extract more heat from the sand.

The temperature of the unit's hot end (and of the outlet air) during a discharge cycle influences the performance of the expanders that are located downstream of the unit. Expanders are sensitive to temperature variations in their inlet temperature, but they can be tuned to operate efficiently over a small range of inlet temperatures. However, if this range is wide, the machines will perform sub optimally, which in turn will lower the overall efficiency of the CAES system. Minimising the temperature drop of the TES + HX unit's hot end is important.

In Fig. 24(B) we can see that the cold end of a design with a wider disc spacing will reach a higher temperature during a charge cycle. This is due to a reduced ability to transfer heat effectively to the sand. The temperature rise in the cold end of a unit is directly proportional to the disc spacing.

The temperature profiles shown in Figs. 23 and 24 reinforce the trends presented in Fig. 19. The roundtrip exergy efficiency of a TES + HX unit will improve as more heat transfer discs are used in the array.

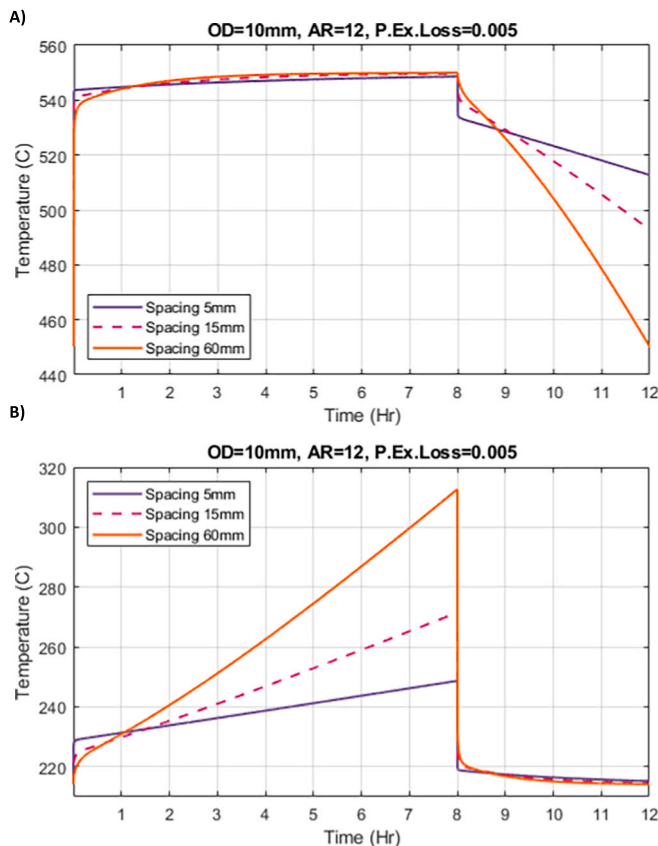


Fig. 24. Temperature of the air at the hot (A) and cold (B) ends of the TES + HX unit throughout a full work cycle.

### 6.3. Effect of varying the pipe diameter

This section explores the effect of varying the outer diameter of the pipes with respect to the reference value of 10 mm. We study diameters of 7.5 mm and 20 mm. The spacing between heat transfer discs is fixed at 15 mm, as it was found to lead to the lowest LCoS for a pipe OD of 10 mm.

Exploring pipe diameters smaller than 7.5 mm is impractical due to much longer simulation times which are caused by the very small spatial and temporal discretisation that is required.

Fig. 25 shows how the levelized costs of storage achieved by different designs vary with respect to the OD of the pipes. Regardless of the pipe diameter, we can see the same general behaviour described in previous sections. TES + HX units based on larger AR achieve lower LCoS due to their increased air-to-steel contact area and a reduced distance between pipe centres, which minimises the distance that heat travels through the sand.

Designs based on small values of  $\Omega$  have excellent exergy efficiencies because: 1) less exergy is lost as pressure drops and 2) there is more surface area due to a greater number of pipes. However, their capital cost is too high and so is their LCoS. Designs based on large values of  $\Omega$  also have high levelized costs due to their low efficiencies, which are caused by a reduced number of pipes and a greater pressure drop.

Fig. 25 shows a red, horizontal line at 35.03 \$/MWh. This is the lowest LCoS achieved by the most cost-effective design based on a pipe OD of 10 mm (Section 6.1). This design considers an AR = 12, an  $\Omega$  of 0.01 and a disc spacing of 15 mm.

We can see in the figure that both, increasing and reducing the OD of the pipes, results in an increased LCoS. The most cost-effective design based on a pipe OD of 7.5 mm (AR = 12 and  $\Omega = 0.031$ ) achieves a LCoS of 35.21 £/MWh. A relatively small increase over the reference value. On the other hand, the best design using 20 mm pipes (AR = 12,  $\Omega = 0.0014$ ) achieves a LCoS of 36.49 £/MWh.

The variation in the levelized costs of different designs comes from a trade-of between efficiency and capital cost. Designs that use bigger pipes have lower capital costs because fewer pipes are needed, which translates into a smaller mass of steel. However, this reduces their heat transfer capabilities and exergy efficiency. Designs that use smaller pipes have higher capital costs due to the increased mass of steel used for their construction, but they achieve considerably higher efficiencies.

The most cost-effective design based on 7 mm OD pipes achieves an efficiency of 91.7 %, while the design that achieves the lowest LCoS using 20 mm pipes has a lower efficiency of 87.6 %.

Fig. 26 shows a set of efficiency curves for designs considering a pipe OD of 7 mm and a pipe OD of 20 mm. As mentioned, the spacing

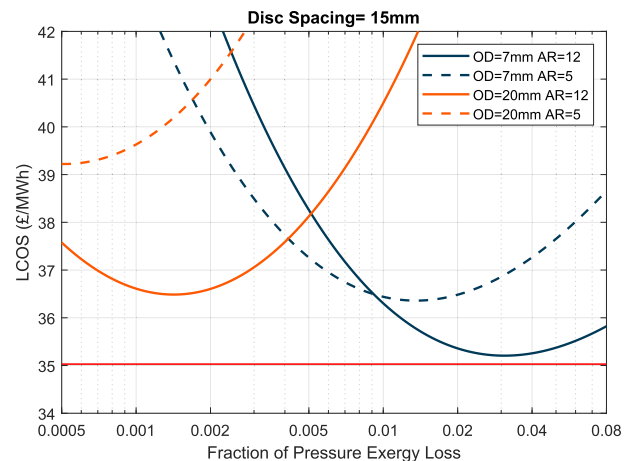


Fig. 25. Effect of the pipe OD on the LCoS of a TES + HX units Disc spacing is fixed at 15 mm.

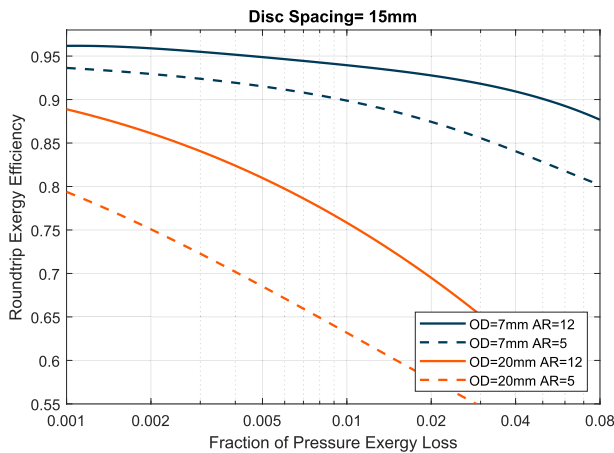


Fig. 26. Effect that changing the pipe diameter has on the roundtrip exergy efficiency of a TES + HX unit.

between discs is fixed at 15 mm. The plot can be compared against the efficiencies achieved with a pipe OD of 10 mm, which have been shown in Fig. 13.

We can see that increasing the pipe OD from 10 to 20 mm has a dramatic impact on the efficiency of a TES + HX unit. For example, considering an aspect ratio of 12, increasing the pipe OD from 10 to 20 mm will cause the efficiency of the unit to reduce between 6 and 20 % points, depending on the specific value of  $\Omega$ .

The highest efficiency attainable with a pipe OD of 20 mm is 92.5 %. However, this requires a very small fraction of pressure exergy loss ( $1 \times 10^{-4}$ ) to compensate for the reduced heat transfer capability of the unit. Such design considers an AR of 12 and a disc spacing of 15 mm.

Considering an  $\Omega$  of 0.001, which is the minimum considered for the other pipe diameters, a unit based on 20 mm pipes achieves an efficiency of 88.9 %. A TES + HX unit will achieve a much higher roundtrip efficiency of 96.2 % for the same allowable fraction of pressure exergy loss ( $1 \times 10^{-3}$ ), when pipes with an OD of 7 mm are used.

Fig. 27 shows how the total heat transfer of the unit is modified as the diameter of the pipes varies. The graph shows the total steel-sand contact area. The heat transfer area is inversely proportional to the pipe OD. This is owed to the fact that for any given value of  $\Omega$ , fewer pipes are needed to achieve the required pressure drop as OD increases. Although the outer surface area of each individual pipe increases, the overall surface area of the array reduces.

As discussed in Section 6.2, for a given pipe OD, the surface area provided by the heat transfer discs varies little with respect to AR or  $\Omega$ . The slight variations are owed to the pipe void centres. When the OD is increased or reduced, the cross section of those void spaces changes but

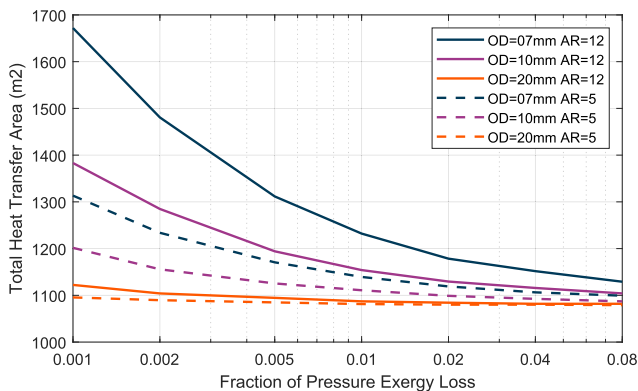


Fig. 27. Variation in the steel-sand heat transfer area with respect to the diameter of the pipes.

the number of pipes also varies. The surface area provided by the heat transfer discs is maximised for a pipe OD = 10 mm, while it reduces for diameters of 7 mm and 20 mm.

The contribution of the heat transfer discs to the total heat transfer area (steel-sand) increases as the pipe OD increases because there are fewer pipes in the array. In a design based on 10 mm pipes, an aspect ratio of 12 and an  $\Omega$  of 0.001 (which is the design that minimises *LCoS*), the discs represent approximately 75 % of the total heat transfer area.

Fig. 28 shows how the number of pipes in the array changes with respect to the pipe OD, aspect ratio and the value of  $\Omega$ . For any given combination of AR and  $\Omega$ , more pipes are needed as the OD reduces. This is to keep the pressure drop below the specified level.

Regardless of the AR and allowable fraction of pressure exergy loss of a unit, the number of pipes increases by a factor  $\sim 2.25$  when the pipe OD reduces from 10 mm down to 7 mm. The number of pipes reduces by factor of  $\sim 0.14$  when the pipe OD increases from 10 mm to 20 mm.

The most cost-effective design (i.e. lowest *LCoS*) considering a 10 mm pipe OD requires 289 pipes. Keeping  $\Omega$  constant at 0.015, the number of pipes in the array increases to 558 if 7 mm pipes are used while it reduces to only 30 pipes for an OD of 20 mm.

Fig. 29 shows how the total cost of fabrication of a TES + HX unit changes with respect to the diameter of the pipes. The capex of a unit is directly proportional to its AR and inversely proportional to  $\Omega$ . Larger aspect ratios and smaller values of  $\Omega$  have higher costs because they need more pipes.

For any given combination between AR,  $\Omega$  and disc spacing (fixed at 15 mm in this section), the capex of a TES + HX unit reduces as the diameter of the pipes increases because fewer pipes are needed. A reduction in the number of pipes reduces all three cost drivers: mass of steel, welding costs, and the cost of x-ray inspection of the welded joints.

The most cost-effective design considering a pipe OD of 10 mm has a capital cost of  $\sim \pounds 38.5k$ . This design is based on an aspect ratio of 12, a pressure exergy loss of  $\sim 0.01$  and a disc spacing of 15 mm. The total cost of fabrication will increase to  $\sim \pounds 50.1k$  if the pipe OD reduces to 7 mm. On the contrary, the cost of this unit will reduce to  $\sim \pounds 21.9k$  if 20 mm pipes were used.

Figs. 26-29 explain why the *LCoS* of a TES + HX unit increases as the diameter of the pipes moves away—in either direction—from the reference value of 10 mm. When 7 mm pipes are used, the efficiency gains are overshadowed by the increase in capital cost. On the other hand, when 20 mm pipes are used, the cost savings are not enough to justify the steep drop in efficiency.

Fig. 30 shows the temperature profiles of three different TES + HX units using 7.5, 10 and 20 mm pipes. All three designs consider the same

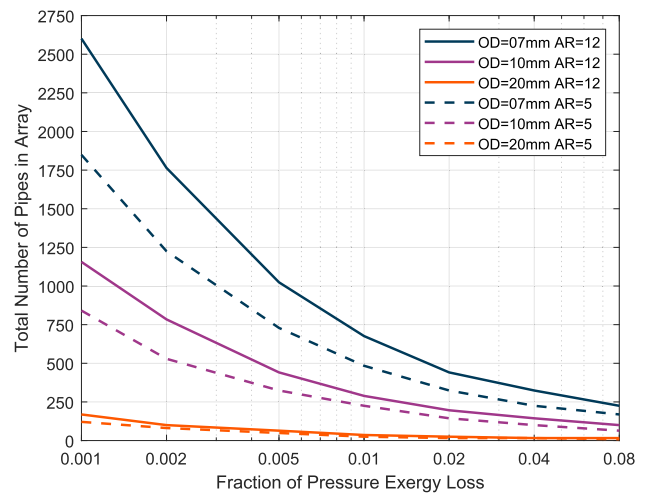


Fig. 28. Comparison of the number of pipes used by designs based on different parameters.

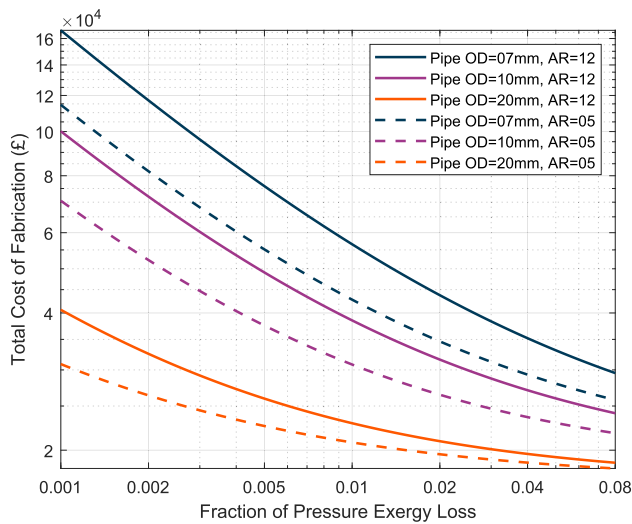


Fig. 29. Effect of the pipe diameter on the total capital cost of a TES + HX unit.

aspect ratio (12, which has been shown to maximise efficiency and minimise *LCoS*), fraction of pressure exergy loss (0.005) and disc spacing (15 mm).

We can see that the thermal gradients worsen as the pipe OD increases. As discussed in Sections 6.1 and 6.2, there are two ways to quantify this. One way is to measure the difference between the temperature profiles of the sand and the air. For this we use the curves at the end of a charge cycle. The unit that uses 7.5 mm pipes shows a mean temperature difference between the sand and air profiles of 7.4°. This difference increases to 11.4° for a pipe OD of 10 mm and to 35.5° for a pipe OD of 20 mm.

The other way is to measure the temperature of the cold end of the thermal store at the end of a charge cycle. The cold end of a TES + HX unit that uses 7 mm pipes reaches 263 °C at the end of the charge, which is 49° above the nominal value. This delta increases to 57° for a pipe OD of 10 mm and to 107° for a pipe OD of 20 mm.

#### 6.4. Best performing unit and benefits to CAES system

This section provides a summary of the geometric and performance parameters of the most cost-effective design found. Here we also discuss the benefits it can provide to a CAES system.

The TES + HX unit design that achieves the lowest possible levelized cost of storage of 35.03 £/MWh is based on:

- an aspect ratio of 12
- a nominal pipe diameter of 10 mm
- a heat transfer disc (or fin) spacing of 15 mm
- a fraction of pressure exergy loss ( $\Omega$ ) of 0.01

The TES + HX unit uses 29.1 tons of silica sand to store ~1 MWh of heat between 215 °C and 550 °C. This includes a mass-overrating factor of 3 and equates to a volume of 10.98 m<sup>3</sup>. Considering an aspect ratio of 12, this volume translates into a 11.65 m long, 0.97 m wide and 0.97 m deep envelope.

The design considers 289 pipes arranged in a square grid of 16 by 16. A third of these pipes hold low-pressure air at ~6.3 bar, a third holds intermediate pressure air at ~40 bar and the remaining third holds high-pressure air at 250 bar.

All the pipes have an outer diameter of 10 mm, and their wall is sized for a pressure of 250 bar. The ease of manufacture given by having equal pipes throughout the array is preferable over the steel savings that could be had. All three pressure levels have the same mass flow rate, which is 0.244 kg/s at full power. Therefore, all the pipes in the array see

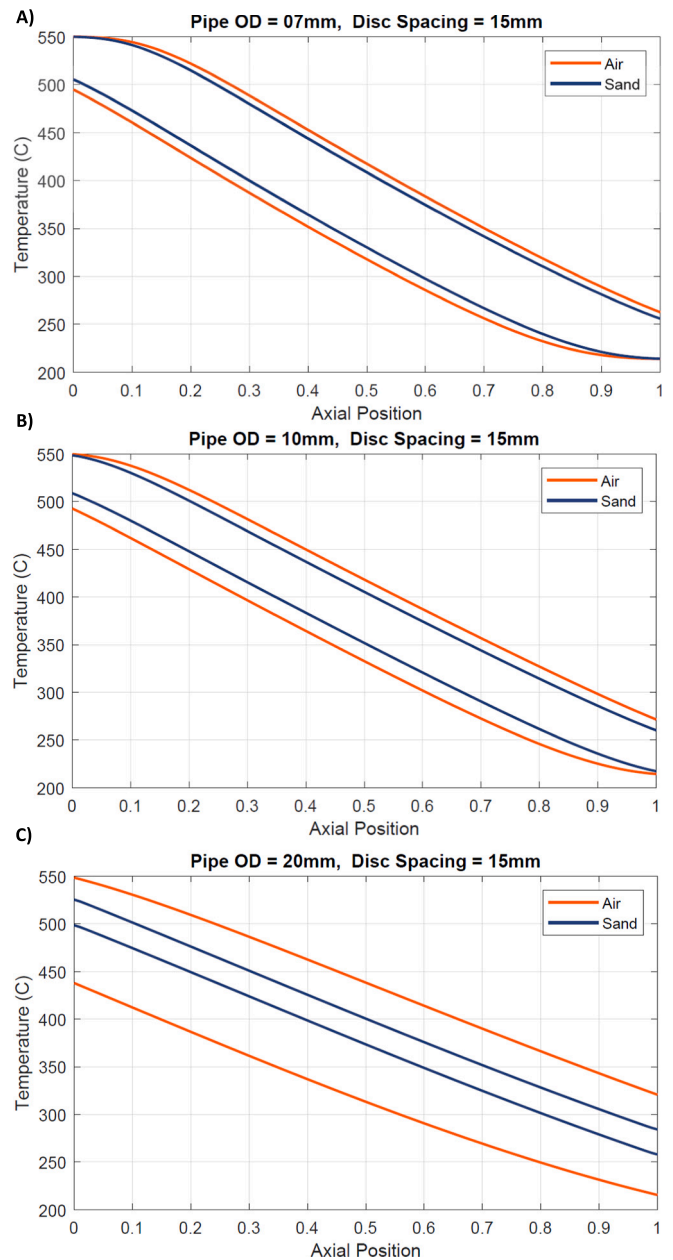


Fig. 30. Temperature profiles at the start and end of a charge cycle for units with different diameter pipes. All three designs consider an aspect ratio of 12, an  $\Omega$  of 0.005 and a disc spacing of 15 mm.

the same air flow rate of  $2.53 \times 10^{-3}$  kg/s.

The heat transfer discs have a thickness of 1 mm and a diameter of 57.1 mm (width of unit/square root of no. of pipes). The separation between them is 15 mm.

Considering this geometry and a stainless-steel density of 8000 kg/m<sup>3</sup>, the TES + HX unit uses approximately 5520 kg of steel. The pipes account for 25 % of the mass, while the heat transfer discs contribute the other 75 %.

The integrated TES + HX unit has a steel-to-sand contact area of ~1147 m<sup>2</sup>. ~90 % of the total area is provided by the heat transfer discs, while the remaining 10 % is owed to outer surface of the pipes. The available steel-sand contact area is equivalent to ~25.4 kg of sand per m<sup>2</sup> of steel surface.

The array of pipes offers an internal surface of approximately 79.4 m<sup>2</sup>, which is equivalent to 108.5 m<sup>2</sup> per kg of air. Considering the above, this design has an external-to-internal area ratio of 14.4. Table 1

**Table 1**

Summary of design parameters of the configuration for an integrated TES + HX unit that minimises the levelized cost of storage.

	Parameter		Unit	
Geometrical	Aspect ratio	12		
	Container width and height	0.97	m	
	Container length	11.65	m	
	Pipe OD (nominal)	10	mm	
	Disc spacing	15	mm	
	Diameter of discs (fins)	57.1	mm	
	Total mass of sand	29,089	kg	
	Volume of sand	10.98	m <sup>3</sup>	
	Number of pipes	289		
	Mass of steel	5521	kg	
	Steel-sand contact area	1147	m <sup>2</sup>	
	Air-steel contact area	79.4	m <sup>2</sup>	
	Operational	Nominal hot side temp.	550	°C
		Nominal cold side temp.	214	°C
		Sand mean Cp in temp. range	1.11	kJ/kg-K
Allowable fraction of pressure exergy loss ( $\Omega$ )		0.01		
Total mass flow of air		0.732	kg/s	
Mass flow of air per pipe	$2.53 \times 10^{-3}$	kg/s		

summarises the geometric and design parameters discussed above.

As mentioned in Section 1, the TES + HX unit will operate within a CAES system which has a power rating of 250 kW and a storage capacity of 1 MWh (4 h of discharge).

In such system, ambient air is preheated to  $\sim 214$  °C and compressed in three stages up to a final pressure of 250 bar. After emerging from each compression stage at a temperature of 550 °C, the stream of pressurised air flows through the TES + HX. The work cycle considered consists of an 8-h charge phase at half power (i.e. half mass flow of air) followed by a 4 h discharge at full power.

Throughout a charge cycle,  $\sim 1.02$  MWh of exergy are passed through the TES + HX. Of these, 567 kWh are in the form of heat (between 214 °C and 550 °C) and the remaining 452 kWh are in the form of pressure-exergy. Each one of the three streams of compressed air at different pressure levels (6, 40 and 250 bar) contribute a third of the total pressure exergy that flows through the thermal store.

The CAES system stores 55.7 % of the exergy in the form of heat and 44.3 % in the form of pressure exergy. The TES + HX unit sees this same exergy split.

During the discharge cycle, preheated air at 214 °C enters the TES + HX unit through the 'cold' side. The exergy content of this air is not accounted for as it is below the temperature bracket of interest (214–550 °C). During the discharge cycle, another 452 kWh in the form of pressure-exergy are passed through the TES + HX unit.

At the end of a charge phase, the 'cold end' temperature of the most cost-effective reaches  $\sim 275$  °C. This represents an exergy loss (exhaust loss) of 50.86 kWh or  $\sim 5$  % of the total exergy passed through the TES + HX unit.

Due to the continuous transfer of heat between air, steel and sand throughout the work cycle and the irreversibilities associated with this, the TES + HX unit sees  $\sim 28.46$  kWh of heat transfer exergy losses, which represent  $\sim 2.8$  % of the total exergy input during a charge.

During a discharge cycle the hot end temperature drops from the nominal value of 550 °C. This is a consequence of the heat transfer and exhaust exergy losses. At the end of the discharge cycle, the temperature of the hot end of the unit will have reduced to 488.8 °C. This temperature drop is comparable in magnitude to the increase of the cold end temperature during the charge phase.

During the 4-hour discharge phase, the TES + HX unit returns 488 kWh of heat-exergy in the temperature bracket [214–550 °C]. This translates into a roundtrip thermal efficiency of 86 %. This figure does not account for pressure-exergy losses.

During a charge cycle the unit has pressure drops of 7.6 kPa, 1.2 kPa and 0.2 kPa in the low, intermediate, and high-pressure air streams, respectively. This translates into a pressure-exergy loss of 0.956 kWh.

Pressure drops are higher during a discharge cycle because the air mass flow is doubled. In this case, the low-pressure air stream sees a pressure drop of 25.9 kPa, while the intermediate and high-pressure streams see pressure drops of 4.1 kPa and 0.66 kPa, respectively. This translates into a combined pressure-exergy loss of 3.174 kWh.

The total roundtrip pressure-exergy loss is therefore  $\sim 4.13$  kWh. This is a small fraction ( $\sim 0.009$ ) of the pressure-exergy input during a charge cycle, which aligns with the specified value of  $\Omega$ . The roundtrip pressure exergy loss of 4.1 kWh is  $\sim 0.4$  % of the total exergy input during a charge cycle.

Considering all the heat-exergy and pressure-exergy losses discussed above, the TES + HX unit achieves an overall roundtrip exergy efficiency of 91.8 %. Table 2 provides a summary of the operational and performance parameters of the best design found, as well as a breakdown of the exergy losses discussed above.

This design has a capital cost of  $\sim$ £38.5k. The mass of steel used for the construction accounts for  $\sim 58$  % of this. The cost of welding the pipes to manifolds on both ends of the unit contributes  $\sim 26$  % of the total cost, while the remaining  $\sim 15$  % is due to the cost of inspecting those welds with x-rays. Considering the overall exergy efficiency mentioned above, the TES + HX unit achieves a LCoS of 35.08 £/MWh (Fig. 12).

The integrated TES + HX unit replaces the thermal store (packed bed of rocks) and the three heat exchangers of a CAES system, as shown in Figs. 1 and 5.

Typically, a packed bed with a capacity of 1MWh and similar operating temperatures would have a cost of approximately £40k. The three heat exchangers (intercoolers) in the system can cost around £100k. These figures were obtained from a medium-scale medium-duration CAES pilot system being developed in the UK.

**Table 2**

Operational and performance parameters of the TES + HX unit and wider CAES system.

	Parameter		Unit
CAES system	CAES system power	250	kW
	Storage capacity	1	MWh
	Compression stages	3	
	Low pressure	6.36	bar
	Intermediate pressure	39.8	bar
	High pressure	250	bar
	Preheat temperature	214	°C
	Compressor outlet temp.	550	°C
	Exergy input to TES + HX unit	1020	kWh
	Input as thermal exergy above preheat temperature	567	kWh
	Pressure exergy input during charge	452	kWh
	Temperature of cold end at end of charge	275	°C
	Temperature of hot end at end of discharge	488	°C
	Exhaust exergy losses	50.86	kWh
	Heat transfer exergy losses	28.46	kWh
TES+ HX unit performance parameters	Heat-exergy discharged (above preheat temperature)	488	kWh
	Stage 1 P. drop at full flow	25.9	kPa
	Stage 2 P. drop at full flow	4.1	kPa
	Stage 3 P. drop at full flow	0.66	kPa
	Pressure exergy loss during charge	0.956	kWh
	Pressure exergy loss during discharge	3.174	kWh
	Total pressure exergy losses	4.13	kWh
	Roundtrip thermal efficiency	86	%
	Overall roundtrip exergy efficiency	91.8	%

**Table 3**

A techno-economical comparison between a TES + HX unit (most cost-effective design) and the heat storage subsystem of a CAES system of equivalent capacity.

Parameters	TES + HX unit	CAES heat storage subsystem
Temp. drop of hot end of thermal store at end of discharge (°C)	62	28
Temperature difference between hot sides of the HXs (°C)	–	15
Roundtrip heat-exergy losses in all 3 heat exchangers (kWh)	–	76.8
Roundtrip heat-exergy losses in the main thermal store (kWh)	79.3	6.9
Roundtrip pressure-exergy losses in tubes, all stages (kWh)	4.1	0.09
Roundtrip pressure-exergy losses in HXs shells, all stages (kWh)	–	10.7
Roundtrip pressure-exergy loss across main thermal store (kWh)	–	21.8
Total roundtrip exergy losses (kWh)	83.4	116.3
Total heat-exergy input during a charge cycle (kWh)	567	585
Total pressure-exergy input during a charge cycle (kWh)	452	484.7
Thermal exergy efficiency (%)	86	85.2
Overall exergy efficiency (%)	91.8	88.9
CapEx (£)	38.5k	147k
LCoS (£/MWh)	35	48.5

An integrated TES + HX is directly charged by the stream of compressed air, therefore it also eliminates the need for a secondary loop of ambient pressure air. This removes an air blower from the system, together with some valves, pipe runs and thermal insulation.

A blower (and variable speed drive) for the flow rates and operating temperatures required can cost up to £7k. Furthermore, to overcome the substantial pressure drop inside the packed bed, the blower can consume as much as 10 kW, which is a noticeable fraction of the system's total discharge power.

The costs of the pipe lengths that can be avoided and the thermal insulation are harder to quantify. However, another advantage of an integrated TES + HX unit is the potential to cut down heat losses by reducing the number and length of the pipes in the system, thus improving the overall efficiency of the CAES system.

Considering a packed bed, three heat exchangers and an air blower, with a combined cost of ~£147k, an integrated TES + HX unit with a capital cost of ~£38.5k offers significant savings (>£108k). There is the potential for further savings based on fewer valves and shorter pipe lengths.

The proposed design can be installed either vertically or horizontally. A horizontal installation is possible—unlike a packed bed—because the air flow is contained within pipes, which eliminates adverse buoyancy effects that distort the thermal gradient. A horizontal installation will increase the footprint. However, it can simplify the commissioning works.

A typical heat storage subsystem of a CAES system, comprising a packed bed of gravel, three heat exchangers and an ambient-pressure blower achieves efficiencies of approximately 89 %. Well-designed packed beds can reach roundtrip thermal exergy efficiencies >98 % [47,48]. This figure—same as the figures reported for the TES + HX unit—does not account for losses to the environment. However, these can be minimised using effective insulation.

For an exergy input of 1.02 MWh, the overall efficiency of ~89 % of the heat storage subsystem accounts for: the thermal exergy losses of the packed bed (~6kWh), roundtrip heat exergy losses all three heat exchangers (~76 kWh), roundtrip pressure-exergy losses in all three heat exchangers (~10 kWh), which are dominated by losses in the ambient side, and the pumping load across the packed bed (21 kWh). The overall efficiency figure does not include heat losses in the pipe runs connecting the compressors to heat exchangers and in the ambient-pressure air loop moving heat to/from the thermal store.

With a combined capital cost of ~£147k and total losses of 113 kWh for the same 1.02 MWh of exergy input, the more conventional heat storage subsystem of a CAES system achieves a LCoS of 48.5 £/MWh, which is ~38 % greater than the LCoS achieved by the integrated TES + HX unit (35.08 £/MWh).

Table 3 provides a comparison between the most cost-effective design for a TES + HX unit and the 'heat storage subsystem' of a medium-scale and medium-duration CAES system. As mentioned, not

many commercial CAES systems exist yet. However, several companies and research institutions are developing pilot plants. The technical and economic data used for this paper comes from a pre-commercial medium-duration medium-scale pilot system. This system has been described in Section 1.

In comparison to the heat storage subsystem used as a benchmark, the TES + HX unit proposed in this paper has a lower capital cost, achieves a higher roundtrip exergy efficiency and offers a lower levelized cost of storage. In addition to that, it simplifies the physical configuration of the system.

Comparing the proposed TES + HX unit with the heat storage subsystem that it replaces provides valuable information. A full-system simulation is necessary to gain a complete understanding of how a CAES system can benefit from using a TES + HX unit. This modelling work will not only provide data about the pros and cons of the replacing the packed bed and heat exchangers for an integrated TES + HX unit (e.g. we can analyse the behaviour of the expanders when subjected to a gradually decreasing inlet temperature) but it will also inform what overall roundtrip efficiency (i.e. electricity -to electricity) the CAES system can achieve. This simulation work falls beyond the scope of this paper but will be addressed in future work.

## 7. Concluding remarks

This paper discusses the design and optimisation of a heat store for a compressed air energy storage (CAES) system. The heat store has integrated heat exchangers, which enables it to be charged directly by the stream of compressed air of the CAES system. The goal is to improve the cost-effectiveness of CAES systems and simplify their architecture.

A typical medium-scale, medium duration CAES system is used as a case study. This system has a discharge power of 250 kWh and a storage capacity of 1 MWh. The TES unit for this type of system operates between 214 °C and 550 °C.

The concept proposed for the integrated TES + HX unit uses silica sand as the heat storage medium. Four design variables are investigated: the diameter of the pipes, the spacing between heat transfer discs, the aspect ratio of the unit and an allowable fraction of pressure-exergy loss.

It is found that designs based on larger aspect ratios and small fractions of pressure-exergy loss achieve high exergy efficiencies due to an increased steel-sand contact area. However, such designs also have an increased capital cost. Reducing the spacing between heat transfer discs also improves the efficiency of a unit by increasing the heat transfer area. However, the efficiency gains are overshadowed by a much greater increase in cost.

The design that achieves the lowest 'levelized cost of storage' (LCoS) of 35.08 £/MWh is based on an aspect ratio of 12 and uses 289 pipes with a diameter of 10 mm. The discs are spaced 15 mm. This design has a capital cost of ~£38.5k. The cost comprises the cost of the stainless steel used for the construction, the cost of welding the pipes to manifolds on

both ends of the unit and the cost of inspecting those welds through x-rays.

The most cost-effective design achieves a thermal exergy efficiency of 86 % and an overall roundtrip exergy efficiency of 91.8 %. During a charge cycle, the unit sees an exergy input of 1.02 MWh; ~55 % of this is heat-exergy and 44 % is in the form of pressure-exergy. The unit can return 488 kWh of heat-exergy during a discharge cycle.

The CAES system used as a case-study utilises a packed bed of gravel as heat store, 3 air-to-air heat exchangers (intercoolers) after each compression stage and a secondary loop of ambient-pressure air to take the heat of compression to the thermal energy store. This heat storage subsystem has an approximate cost of ~£147k and achieves efficiencies of ~89 %. This subsystems achieves a LCoS of 48.5 £/MWh.

With a capital cost of approximately £38.5k, the integrated TES + HX unit offers a significant cost reduction. Additionally, it can improve the efficiency of the subsystem by >2 % points. The lower capital cost and higher overall efficiency enable the TES + HX unit achieve a much lower leveled cost of storage compared to the conventional heat storage subsystem based on a packed bed and heat exchangers. Additionally, a TES + HX can lead to a simpler system architecture. The proposed concept can also work as part of other energy storage systems such as pumped heat energy storage and waste heat recovery systems.

## Declaration of competing interest

The authors confirm that there is no conflict of interest to declare.

## Data availability

No data was used for the research described in the article.

## Acknowledgements

The authors would like to thank the United Kingdom's Engineering and Physical Sciences Research Council (EPSRC) and the Department for Energy Security and Net Zero for supporting this work through the 'Sustainable, Affordable and Viable Compressed Air Energy Storage' (EP/W027569/1) grant and the Energy Entrepreneurs fund, respectively. The authors also express their gratitude to the reviewers who contributed to improving the quality of this paper.

## References

- [1] H. Guo, Y. Xu, M. Yan, H. Kang, L. Cheng, L. Huang, D. Xu, Y. Zhu, H. Chen, Effect of thermal storage and heat exchanger on compressed air energy storage systems, *Adv. Heat Tran.* (2023), <https://doi.org/10.1016/bs.aiht.2023.02.003>.
- [2] L. Bartela, J. Ochmann, S. Waniczek, M. Lutyński, G. Smolnik, S. Rulik, Evaluation of the energy potential of an adiabatic compressed air energy storage system based on a novel thermal energy storage system in a post mining shaft, *J. Energy Storage* 54 (2022), 105282.
- [3] D. Pottier, B. Cardenas, S. Garvey, J. Rouse, E. Hough, A. Bagdanavicius, E. Barbour, Comparative analysis of isochoric and isobaric adiabatic compressed air energy storage, *Energies* 16 (6) (2023) 2646.
- [4] M. Mersch, P. Sapin, A.V. Olympios, Y. Ding, N. Mac Dowell, C.N. Markides, A unified framework for the thermo-economic optimisation of compressed-air energy storage systems with solid and liquid thermal stores, *Energy Convers. Manag.* 287 (2023), 117061.
- [5] X. Zhang, Y. Li, Z. Gao, S. Chen, Y. Xu, H. Chen, Overview of dynamic operation strategies for advanced compressed air energy storage, *J. Energy Storage* 66 (2023), 107408.
- [6] Y. Xu, H. Zhang, F. Yang, L. Tong, D. Yan, Y. Yang, Y. Wang, Y. Wu, Performance of compressed air energy storage system under parallel operation mode of pneumatic motor, *Renew. Energy* 200 (2022) 185–217.
- [7] J. Huang, Y. Xu, H. Guo, X. Geng, H. Chen, Dynamic performance and control scheme of variable-speed compressed air energy storage, *Appl. Energy* 325 (2022), 119338.
- [8] Y. Tian, T. Zhang, N. Xie, Z. Dong, Z. Yu, M. Lyu, Y. Lai, X. Xue, Conventional and advanced exergy analysis of large-scale adiabatic compressed air energy storage system, *J. Energy Storage* 57 (2023), 106165.
- [9] P. Ran, H. Zhang, Y. Qiao, J. Wang, Z. Li, Y. Wang, Thermodynamic analysis for a novel steam injection adiabatic compressed air energy storage hybrid system, *J. Energy Storage* 55 (A) (2022), 105424.
- [10] E. Barbour, D. Pottier, Adiabatic compressed air energy storage technology, *Joule* 5 (8) (2021) 1914–1920.
- [11] H. Wang, Z. Wang, C. Liang, R. Carriveau, W. Xiong, Underwater compressed gas energy storage (UWCGES): current status, challenges, and future perspectives, *Appl. Sci.* 12 (18) (2022) 9361.
- [12] A.V. Olympios, J.D. McTigue, P. Farres-Antunez, C.N. Markides, Progress and prospects of thermo-mechanical energy storage—a critical review, *Prog. Energy* 3 (2021), 022001.
- [13] S. Garvey, A. Pimm, Compressed air energy storage, in: T. Letcher (Ed.), *Storing Energy*, 2nd edn, Elsevier, 2022, pp. 117–140.
- [14] P.E. Dodds, S.D. Garvey, Energy storage options to balance renewable electricity systems, in: T.M. Letcher (Ed.), *Storing Energy*, Elsevier, 2022, ISBN 9780128245101, pp. 13–33.
- [15] B. Cardenas, L. Swinfen-Styles, J. Rouse, A. Hoskin, W. Xu, S.D. Garvey, Energy storage capacity vs. renewable penetration: a study for the UK, *Renew. Energy* 171 (2021) 849–867.
- [16] S. Trevisan, W. Wang, R. Guedez, B. Laumert, Experimental evaluation of a high-temperature radial-flow packed bed thermal energy storage under dynamic mass flow rate, *J. Energy Storage* 54 (2022), 105236.
- [17] S. Singh, K. Sørensen, T. Condra, S.S. Batz, K. Kristensen, Investigation on transient performance of a large-scale packed-bed thermal energy storage, *Appl. Energy* 239 (2019) 1114–1129.
- [18] Y.S. Sun, Y. Han, G.D. Li, H.Y. Shen, X.M. Chi, C.Y. Zhang, Numerical study of high-temperature cascaded packed bed thermal energy storage system, *Case Stud. Therm. Eng.* 37 (2022), 102258.
- [19] S. Trevisan, Y. Jemmal, R. Guedez, B. Laumert, Packed bed thermal energy storage: a novel design methodology including quasi-dynamic boundary conditions and techno-economic optimization, *J. Energy Storage* 36 (2021), 102441.
- [20] K. Rusin, J. Ochmann, L. Bartela, S. Rulik, B. Stanek, M. Jurczyk, S. Waniczek, Influence of geometrical dimensions and particle diameter on exergy performance of packed-bed thermal energy storage, *Energy* 260 (2022), 125204.
- [21] H. Zhou, Z. Lai, K. Cen, Experimental study on energy storage performances of packed bed with different solid materials, *Energy* 246 (2022), 123416.
- [22] J. Ochmann, K. Rusin, S. Rulik, S. Waniczek, L. Bartela, Experimental and computational analysis of packed-bed thermal energy storage tank designed for adiabatic compressed air energy storage system, *Appl. Therm. Eng.* 213 (2022), 118750.
- [23] M. von der Heyde, G. Schmitz, Electric thermal energy storage based on packed bed, in: *Encyclopedia of Energy Storage* 2, 2022, pp. 108–121.
- [24] W. Guo, Z. He, A. Mawire, P. Zhang, Parametric investigation of charging and discharging performances of a cascaded packed bed thermal energy storage system, *J. Energy Storage* 57 (2023), 106229.
- [25] M. Al-Azawii, S.F.H. Alhamdi, S. Braun, J.F. Hoffmann, N. Calvet, R. Anderson, Experimental study on packed-bed thermal energy storage using recycled ceramic as filler materials, *J. Energy Storage* 44 (A) (2021), 103375.
- [26] B. Kocak, H. Paksoy, Performance of laboratory scale packed-bed thermal energy storage using new demolition waste based sensible heat materials for industrial solar applications, *Sol. Energy* 211 (2020) 1335–1346.
- [27] D. Laing, D. Lehmann, C. Bahl, Concrete storage for solar thermal power plants and industrial process heat, in: *IRES III 2008, 3rd International Renewable Energy Storage Conference*, 2008. Berlin.
- [28] D. Laing, W.D. Steinmann, M. Fiß, R. Tamme, T. Brand, C. Bahl, Solid media thermal storage development and analysis of modular storage operation concepts for parabolic trough power plants, *J. Sol. Energy Eng.* 130 (1) (2008), 011006.
- [29] D. Laing, C. Bahl, T. Bauer, D. Lehmann, W.D. Steinmann, Thermal energy storage for direct steam generation, *Sol. Energy* 85 (4) (2011) 627–633.
- [30] D. Laing, D. Lehmann, M. Fiß, C. Bahl, Test results of concrete thermal energy storage for parabolic trough power plants, *J. Solar Energy Eng.* 131 (2009), 041007-1.
- [31] N. Hoivik, C. Greiner, E. Bellido-Tirado, J. Barragan, P. Bergan, G. Skeie, P. Blanco, N. Calvet, Demonstration of Energy Nest thermal energy storage (TES) technology. Solar-PACES, in: *AIP Conf. Proc.* 1850, 2016, pp. 080011-1–080011-8.
- [32] C. Nils Hoivik, J. Greiner, A. Crespo Barragan, G. Iniesta, P. Skeie, P. Bergan, N. Calvet Blanco-Rodriguez, Long-term performance results of concrete-based modular thermal energy storage system, *J. Energy Storage* 24 (2019), 100735.
- [33] T. Baumann, S. Zunft, Properties of granular materials as heat transfer and storage medium in CSP application, *Sol. Energy Mater. Sol. Cells* 143 (2015) 38–47.
- [34] M. Diago, A.C. Iniesta, T. Delclos, T. Shamim, N. Calvet, Characterization of desert sand for its feasible use as thermal energy, *Energy Procedia* 75 (2015), 2133–2118.
- [35] M. Diago, A.C. Iniesta, A. Soum-Glaude, N. Calvet, Characterization of desert sand to be used as a high-temperature thermal energy storage medium in particle solar receiver technology, *Appl. Energy* 216 (2018) 402–413.
- [36] M. Diago, A.C. Iniesta, Q. Falcoz, T. Shamim, N. Calvet, Energy and exergy analysis of a novel gravity-fed solid particle solar receiver, *Energy Procedia* 69 (2015) 812–821.
- [37] A.C. Iniesta, M. Diago, T. Delclos, Q. Falcoz, T. Shamim, N. Calvet, Gravity-fed combined solar receiver/storage system using sand particles as heat collector, heat transfer and thermal energy storage media, *Energy Procedia* 69 (2015) 802–811.
- [38] K. Schwaiger, M. Haider, M. Hämmerle, D. Wünsch, M. Obermaier, M. Beck, A. Niederer, S. Bachinger, D. Radler, C. Mahr, R. Eisl, F. Holzleitner, sandTES – an active thermal energy storage system based on the fluidization of powders, *Energy Procedia* 49 (2014) 983–992.
- [39] B. Xu, J. Han, A. Kumar, P. Li, Y. Yang, Thermal storage using sand saturated by thermal-conductive fluid and comparison with the use of concrete, *J. Energy Storage* 13 (2017) 85–95.

- [40] S. Alaqel, A. El-Leathy, H. Al-Ansary, E. Djajadiwinata, N. Saleh, S. Danish, R. Saeed, A. Alswaiyd, Z. Al-Suhaibani, S. Jeter, A. Al-Balawif, F. Al-Harhi, Experimental investigation of the performance of a shell-and-tube particle to air heat exchanger, *Sol. Energy* 204 (2020) 561–568.
- [41] C.S. Kim, *Thermophysical Properties of Stainless Steels*, Argonne National Laboratory, Illinois, USA, 1975.
- [42] J. J. Valencia, *Thermophysical Properties ASM Handbook, Volume 15: Casting ASM Handbook Committee*, p 468–481 DOI: <https://doi.org/10.1361/asmhba0005240>.
- [43] P. Richet, Y. Bottinga, L. Denielou, J.P. Petitet, C. Tequi, Thermodynamic properties of quartz, cristobalite and amorphous SiO<sub>2</sub>: drop calorimetry measurements between 1000 and 1800 K and a review from 0 to 2000 K, *Geochim. Cosmochim. Acta* 46 (1982) 2639–2658.
- [44] B.S. Hemingway, Quartz: heat capacities from 340 to 1000K and revised values for the thermodynamic properties, *Am. Mineral.* 72 (1987) 273–279.
- [45] E.W. Lemmon, R.T. Jacobsen, S.G. Penoncello, D.G. Friend, Thermodynamic properties of air and mixtures of nitrogen, argon, and oxygen from 60 to 2000 K at pressures to 2000 MPa, *J. Phys. Chem. Ref.* 29 (3) (2000) 331–385.
- [46] E.W. Lemmon, R.T. Jacobsen, Viscosity and thermal conductivity equations for nitrogen, oxygen, argon, and air, *Int. J. Thermophys.* 25 (2004) 21–69.
- [47] B. Cardenas, T.R. Davenne, J.P. Rouse, S.D. Garvey, Effect of design parameters on the exergy efficiency of a utility-scale packed bed, *J. Energy Storage* 18 (2018) 267–284.
- [48] B. Cardenas, T.R. Davenne, J. Wang, Y. Ding, Y. Jin, H. Chen, Y. Wu, S.D. Garvey, Techno-economic optimization of a packed-bed for utility-scale energy storage, *Appl. Therm. Eng.* 153 (2019) 206–220.
- [49] T.R. Davenne, S.D. Garvey, B. Cardenas, M.C. Simpson, The cold store for a pumped thermal energy storage system, *J. Energy Storage* 14 (2) (2017) 295–310.
- [50] Ofgem, Wholesale Market Indicators, Available online: <https://www.ovoenergy.com/guides/energy-guides/wholesale-energy-prices.html>.